第45卷 第1期
2026年1月

岩 石 矿 物 学 杂 志
ACTA PETROLOGICA ET MINERALOGICA

Vol. 45, No. 1: 19~45
Jan., 2026

Doi: 10.20086/j.cnki.yskw.2026.5004

大洋俯冲和陆-陆碰撞过程中陆壳的改造与成熟
——以柴北缘鱼卡地区岩浆和深熔作用为例

孙雯慧[1], 王林涛[1], 蒋晓聪[1], 祁 钰[1], 李传志[1], 王 越[1], 于胜尧[1,2]

(1. 中国海洋大学海底科学与探测技术教育部重点实验室, 山东 青岛 266100; 2. 崂山国家实验室海洋矿产资源评价与探测技术功能实验室, 山东 青岛 266237)

摘 要: 大洋俯冲带与碰撞造山带是大陆地壳演化与成熟的关键位置,但引发地壳改造和成熟的具体机制尚存在诸多争议。本文对柴北缘俯冲碰撞杂岩带拐角梁-双口山弧岩浆-变质单元内的长英质片麻岩及其内部的浅色体、基性片麻岩和闪长岩开展了详细的岩石学、地球化学、锆石 U-Pb 年代学及锆石 Lu-Hf 同位素分析工作,以探讨该区内大陆地壳演化的关键机制。全岩地球化学分析显示,长英质片麻岩、基性片麻岩及闪长岩均富集 LILEs 和 LREEs 而亏损 HFSEs,与典型弧型岩浆岩地球化学特征类似,其中基性片麻岩与长英质片麻岩具有连续演化的主量元素组成,暗示长英质片麻岩原岩或源于基性岩浆的结晶分异;长英质片麻岩中的浅色体具有高 SiO_2、Al_2O_3 和 Na_2O 而低 K_2O、CaO、Rb/Sr 和 Th/U 的奥长花岗岩地球化学特征,与水致部分熔融趋势一致。锆石 U-Pb 定年结果显示,基性片麻岩的原岩与闪长岩分别形成于 470.9±6.5 Ma 与 441.6±3.0 Ma,Hf 同位素分析显示基性片麻岩锆石 εHf(t)值为+6.74~+11.26,闪长岩锆石 εHf(t)值为+5.13~+8.06;长英质片麻岩中的浅色体形成于 441.6±3.5 Ma,锆石 εHf(t)值为+7.24~+12.27,与基性片麻岩基本一致。综合分析表明,拐角梁-双口山弧岩浆-变质单元内记录了两期弧岩浆活动和一期变质-深熔事件:约 470 Ma 的洋壳俯冲阶段,俯冲流体交代地幔楔发生部分熔融,引发了第 1 期弧岩浆活动,从而形成了基性片麻岩与长英质片麻岩的原岩;约 440 Ma 洋壳俯冲到陆-陆碰撞过程中,软流圈上涌,含水地幔部分熔融形成闪长岩,闪长岩在侵位与结晶过程中释放热量与流体导致长英质片麻岩的原岩发生水致熔融。这两期弧岩浆活动及随后的深熔事件均促进了柴北缘俯冲碰撞杂岩带内大陆地壳由基性向酸性的转化,表明由洋壳俯冲到陆-陆碰撞转换过程中的弧岩浆活动及深熔作用或是推动大陆地壳的改造与成熟的关键因素。

关键词: 大陆地壳成熟; 大洋俯冲; 陆-陆碰撞; 混合岩化; 柴北缘

中图分类号: P542; P588.3 **文献标识码**: A **文章编号**: 1000-6524(2026)01-0019-27

Reworking and maturation of continental crust during oceanic subduction and continental collision processes: A case study of magmatism and anatexis in Yuka area, North Qaidam

SUN Wen-hui[1], WANG Lin-tao[1], JIANG Xiao-cong[1], QI Yu[1], LI Chuan-zhi[1], WANG Yue[1] and YU Sheng-yao[1,2]

(1. MOE Key Lab of Submarine Geoscience and Prospecting Techniques, Ocean University of China, Qingdao 266100, China; 2. Laboratory for Marine Mineral Resources, Laoshan Laboratory, Qingdao 266237, China)

Abstract: The oceanic subduction zones and collision orogenic belts are critical regions for the evolution and maturation of continental crust. However, the specific mechanisms driving crustal reworking and maturation remain subjects of considerable controversy. In this study, we employ an integrated approach that combines petrography, geochemistry,

收稿日期: 2025-01-16; **接受日期**: 2025-08-23; **编辑**: 郝艳丽

基金项目: 国家自然科学基金项目(42372247); 泰山学者特聘专家项目(tstp20231214)

作者简介: 孙雯慧(1999-),女,硕士研究生, 地质学专业, E-mail: 1275718923@qq.com; 通讯作者: 王林涛(1995-), 博士研究生, 地质学专业, E-mail: wang_lt@stu.ouc.edu.cn; 蒋晓聪(1998-), 博士研究生,地质学专业, E-mail: 2363964495@qq.com。

zircon U-Pb geochronology, and zircon Lu-Hf isotopic analyses to analyze the felsic gneisses and their internal leucosomes, basic gneisses, and diorites within the Guaijiaoliang-Shuangkoushan arc-related rock unit, in order to investigate the key mechanisms driving continental crust evolution in this region. Whole-rock geochemical analysis reveals that the felsic gneisses, basic gneisses, and diorites are enriched in large ion lithophile elements and light rare earth elements, while being depleted in high field strength elements, characteristic of typical arc magmatic geochemical signatures. The basic and felsic gneisses exhibit a continuous evolution in major element composition, suggesting that the protolith of felsic gneisses originated from the crystallization differentiation of basic magmas. The leucosomes within the felsic gneisses exhibit high SiO_2, Al_2O_3, and Na_2O contents but low K_2O, CaO, Rb/Sr, and Th/U ratios, characteristic of the geochemical features of trondhjemite, consistent with fluid-present melting. Zircon U-Pb geochronology reveals that the protolith of basic gneiss and diorites formed at 470.9±6.5 Ma and 441.6±3.0 Ma, respectively. Hf isotopic analysis reveals that the zircon εHf(t) values of the basic gneisses range from +6.74 to +11.26, whereas the εHf(t) values of the diorites vary from +5.13 to +8.06. The leucosomes in the felsic gneisses crystallized at 441.6±3.5 Ma, and their zircon εHf(t) values range from +7.24 to +12.27, which is consistent with those of the basic gneisses. Comprehensive analysis indicates that the Guaijiaoliang-Shuangkoushan arc magmatic-metamorphic unit records two phases of arc magmatic activity and one phase of metamorphic-anatexis. During the ~470 Ma oceanic crust subduction phase, subducted fluids facilitated partial melting of the mantle wedge, leading to the formation of the first phase of arc magmatism, i.e., the protoliths of the basic gneisses and felsic gneisses. During the transition from oceanic subduction to continental collision at ~440 Ma, the upwelling of the asthenosphere triggered partial melting of a hydrated mantle, resulting in the formation of diorites. The emplacement and crystallization of the diorites released heat and fluids, inducing hydrous partial melting of the felsic gneiss protolith. Both phases of arc magmatic activity and the subsequent anatexis events promoted the transformation of the continental crust from basic to acidic within the North Qaidam subduction-collision mélange belt. This suggests that arc magmatism and anatexis processes during the transition from oceanic subduction to continental collision were key factors driving the reworking and maturation of the continental crust.

Key words: continental crust maturation; oceanic subduction; continental collision; migmatitization; North Qaidam

Fund support: Nation Natural Science Foundation of China (42372247); Taishan Scholars Program (tstp20231214)

大陆地壳具有长时间留存演化的特点,使其成为记录地球演化历史的原始档案馆和最重要的地球化学储库之一(Spencer *et al.*, 2017; Korenaga, 2018)。成熟的大陆地壳具有典型垂直分层结构,由上至下依次为长英质上地壳及镁铁质下地壳(Rudnick, 1995; Rudnick and Gao, 2003; Zhu *et al.*, 2022),总体成分呈英安质或安山质,与原始地壳的基性组成差异显著(Hawkesworth and Kemp, 2006; Hacker *et al.*, 2011)。理解大陆地壳的形成与演化机制是地球科学研究最关键的基本问题之一(Hacker *et al.*, 2011; Niu *et al.*, 2013; Zhang *et al.*, 2014),然而由于地壳形成时多样的地质背景及后期各种改造的叠加,使得探究该问题极具挑战性(Ferreira *et al.*, 2020)。

大陆地壳平均组分与安山质弧岩浆岩具有极大相似性(Rudnick and Gao, 2003; Davidson and Arculus, 2006),故显生宙以来的大陆地壳被认为形成于俯冲带岩浆作用(Rudnick, 1995; Taylor and McLennan, 1995),促使俯冲带成为研究大陆地壳改造和成熟的热点场所(Arculus, 1981; Zheng, 2012)。碰撞造山带(包含大陆俯冲)通常形成于由洋壳俯冲产生大陆弧岩浆的初始阶段到陆-陆碰撞过程中岩石圈的改造阶段(Thompson and Connolly, 1995; Zheng and Gao, 2021; Zhu *et al.*, 2022),带内记录了英安质-安山质大陆地壳的形成、生长和保存的关键动力学过程(Rudnick, 1995; Cawood *et al.*, 2013)。碰撞前的大陆弧岩浆作用记录了洋壳俯冲过程中地幔楔的水化熔融以及新生镁铁质地壳的形成(Taylor and McLennan, 1995),而弧岩浆通过分离结晶作用形成超基性-基性堆晶岩及衍生的中-酸性熔体,由

于密度差异,弧堆晶体通过拆沉作用返回地幔从而推动弧地壳向中性组分转化(Greene *et al.*, 2006; Müntener and Ulmer, 2006; Jagoutz, 2010, 2014)。与之不同的是,陆-陆碰撞则通常导致新生和古老陆壳重熔形成中-酸性熔体,联合后续的地壳混染和岩浆混合等多阶段岩浆演化过程促进大陆地壳走向成熟(Thompson and Connolly, 1995; Zheng and Gao, 2021; 秦圣凯等, 2023)。然而,目前尚不清楚大陆弧区岩石圈的改造如何改变地壳的性质和组成,以及为什么这一过程发生在碰撞造山带(Zhu *et al.*, 2022)。

柴北缘俯冲碰撞杂岩带是一条典型大陆型深俯冲变质带(Zhang *et al.*, 2008a, 2009a, 2009b; Yu *et al.*, 2013),记录了从洋壳俯冲到陆-陆碰撞的完整造山演化史(杨经绥等, 2003; 史仁灯等, 2004, Zhang *et al.*, 2013; Song *et al.*, 2014b; 朱小辉等, 2015)。带内广泛分布洋壳俯冲阶段形成的大陆弧岩浆岩(史仁灯等, 2004; Wu *et al.*, 2009, 2014)以及陆-陆碰撞过程中形成的同碰撞岩浆岩(Wu *et al.*, 2009; Zhao *et al.*, 2017),是研究地壳改造与成熟过程的理想载体。针对这些岩浆岩,前人已开展了大量岩石岩相学、地质年代学以及地球化学分析工作,柴北缘洋壳俯冲与陆-陆碰撞时间分别被厘定为 520~460 Ma 与 455~420 Ma(Yu *et al.*, 2021)。其中,洋壳俯冲阶段的弧岩浆岩从柴北缘西段的赛什腾地区到东段的乌兰地区均有报道,但此阶段的长英质岩浆岩普遍被认为源于先前地壳的重熔,属于地壳改造的范畴(Gao *et al.*, 2022, 2023; 王秉璋等, 2022),而与地壳净生长相关的基性弧岩浆结晶分异成因的中-酸性岩浆岩却鲜有报道。陆-陆碰撞阶段的同碰撞岩浆岩主要出露于都兰、锡铁山、绿梁山及鱼卡地体中,以埃达克质奥长花岗岩和 S 型花岗岩为主(Song *et al.*, 2014a, 2014b; Zhao *et al.*, 2017; Yu *et al.*, 2019b; Yang *et al.*, 2020),这些花岗岩主要源于古老陆壳的重熔,但也有观点认为其形成于大陆地壳及先前俯冲洋壳熔体的混合(Zhao *et al.*, 2017)。由此可见,柴北缘俯冲碰撞杂岩带中尚缺乏洋壳俯冲阶段陆壳生长的相关证据,且陆-陆碰撞阶段地壳再造机制也存在争议。最近,鱼卡-绿梁山地区新被厘定出的拐角梁-双口山弧岩浆-变质单元内保留了大量弧岩浆及深熔作用证据,可能成为解决上述问题的突破口,因而本文在该弧岩浆-变质单元内开展了详细的调查分析工作,以探究柴北缘早古生代大陆地壳演化的关键过程。

1　地质背景

柴北缘俯冲碰撞杂岩带位于柴达木地块与祁连地块之间,呈 NW-SE 向展布,西起塞什腾山,东至都兰北部沙柳河-阿尔茨托山,南与柴达木地块以柴北缘断裂相接,北与祁连地块以宗务隆构造带相隔,与南阿尔金俯冲碰撞杂岩带一同被阿尔金左旋断裂分割(图 1a)。柴北缘俯冲碰撞杂岩带可进一步划分为两个次级单元: 滩间山火山杂岩带和柴北缘高压-超高压变质带,二者呈韧性剪切带或断层接触(张建新等, 2015; Zhou *et al.*, 2022)。其中,柴北缘高压-超高压变质带西起鱼卡地区,东至沙柳河地区,东西延伸约 400 km,主体由正片麻岩、副片麻岩以及少量以似层状或透镜体形式夹于其中的榴辉岩、基性麻粒岩和石榴橄榄岩组成(Yu *et al.*, 2019a, 2019b)。根据岩石组合、变质演化历史等特征的差异,柴北缘高压-超高压变质带可被划分为 4 个次级构造单元(Zhang *et al.*, 2008b),自东向西依次都兰榴辉岩-片麻岩单元、锡铁山榴辉岩-片麻岩单元、绿梁山石榴橄榄岩-片麻岩单元和鱼卡榴辉岩-片麻岩单元(图 1a)。近年来,随着研究工作的深入,原有的划分方案得到进一步的细化和补充,特别是在柴北缘高压-超高压变质带的西段,如 Zhou 等(2022)在绿梁山与鱼卡地体之间新厘定出一个弧岩浆变质单元(图 1b),进而将绿梁山和鱼卡地体划分为 3 个次级变质单元: 小红山-绿梁山高温-超高温变质单元、拐角梁-双口山弧岩浆-变质单元和鱼卡-落风坡中低温-超高压变质单元(图 1b)。

本文研究区位于拐角梁-双口山弧岩浆-变质单元(图 1b)内,该单元包含两套变质程度不同的岩石: 角闪岩相变质岩石组合和浅变质岩石组合。其中,角闪岩相变质岩石组合包含含石榴子石花岗质片麻岩及含石榴子石变辉长-闪长质片麻岩;浅变质岩石组合则主要包含滩间山群浅变质火山碎屑岩、变火山熔岩和少量未变质的辉长岩等,其中辉长岩的结晶年龄为 498~448 Ma(袁桂邦等, 2002; 俞军真等, 2020),可能代表了早期与柴达木洋俯冲有关的弧岩浆活动亦或是 SSZ 蛇绿岩的组成部分。此外,该变质单元内发育有大量未发生变质的奥陶纪-

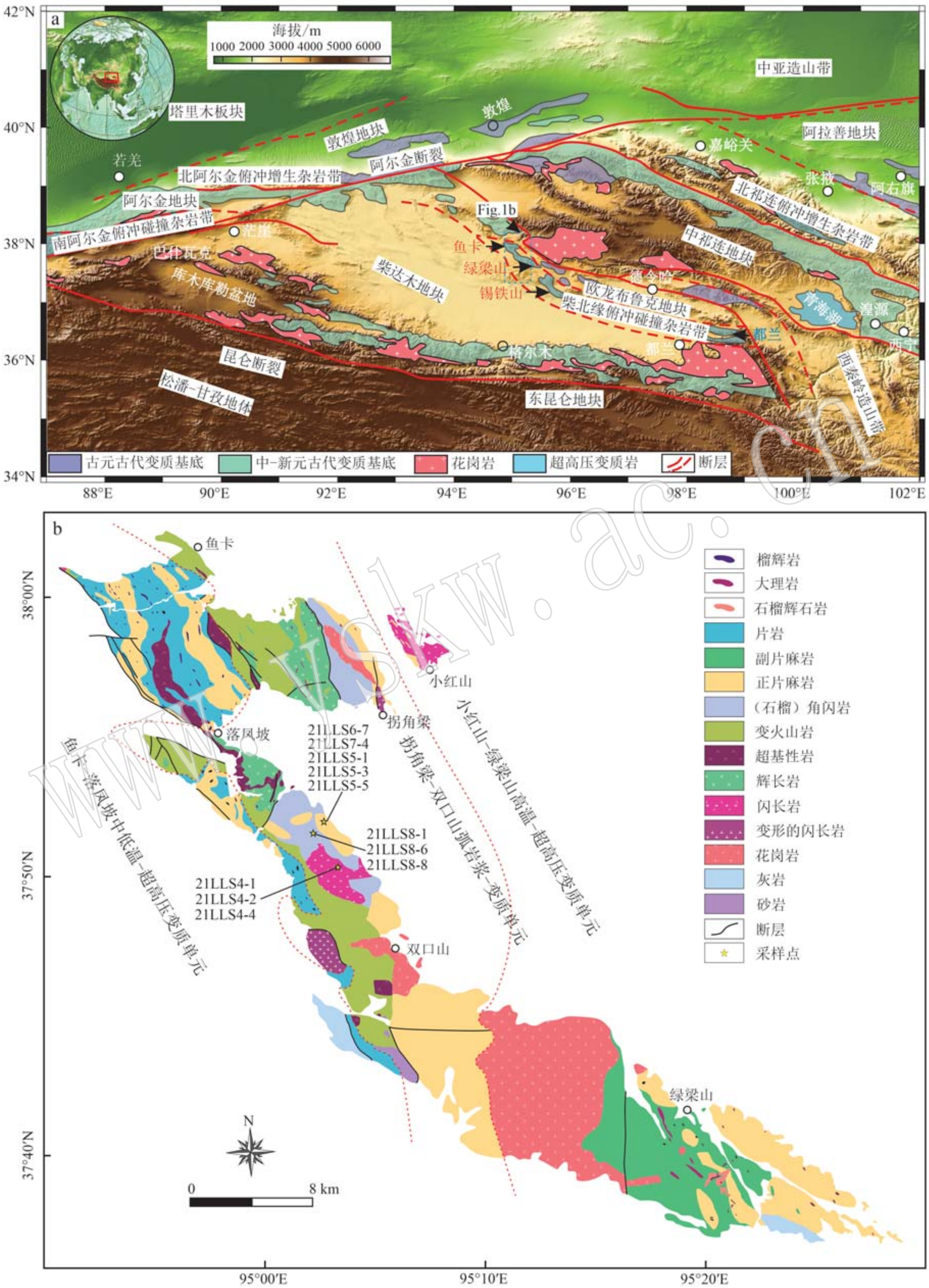

图 1 柴北缘俯冲碰撞杂岩带地质简图(a,据 Zhang *et al.*, 2017 修改)和柴北缘变质带西段地质图(b,据 Zhou *et al.*, 2022 修改)

Fig. 1 Geological sketch map of the North Qaidam subduction-collision mélange belt (a, modified from Zhang *et al.*, 2017) and geological map of the western part of the North Qaidam metamorphic belt (b, modified from Zhou *et al.*, 2022)

志留纪闪长岩(图 1b)。尽管前期调查工作表明该弧岩浆-变质单元或许记录了从洋-陆俯冲向陆-陆碰撞转换过程中弧火山作用和弧中下部岩浆-变质作用的复杂演化历史,但该区域目前尚未有详尽的岩浆和变质研究工作报道。

2　野外关系及样品描述

基性片麻岩与长英质片麻岩呈近似互层状产出,二者分界线并不明确,在接触地带常常以互相夹杂的形式出露(图 2a)。区内的闪长岩与基性片麻岩及长英质片麻岩均呈侵入接触(图 2b)。基性片麻岩与长英质片麻岩的原岩均经历了部分熔融,其中基性片麻岩部分熔融程度相对较低,浅色体以顺层理发育的微细条带产出(图 2c),而长英质片麻岩则经历了强烈的部分熔融改造,多已转变为变熔岩,其与源区浅色体之间边界模糊(图 2d),浅色体中均匀分布有厘米级的角闪石聚集体(图 2e)。闪长岩岩体内部无变形迹象,而岩体边部,存在一定变形,展现出定向性(图 2f)。

基性片麻岩主要由角闪石(35%~40%)、斜长石(25%~30%)、石榴子石(10%~15%)、石英(5%~10%)、绿帘石(约 5%)及少量副矿物如蓝晶石、金红石、钛铁矿等组成(图 3a)。样品中的石榴子石为约 1 mm 半自形的变斑晶,内部包裹体较少,主要为长石及钛铁矿,外部发育白眼圈结构,可能代表退变质过程的降压阶段。基质主要由半自形的角闪石和斜长石以及他形的石英组成。

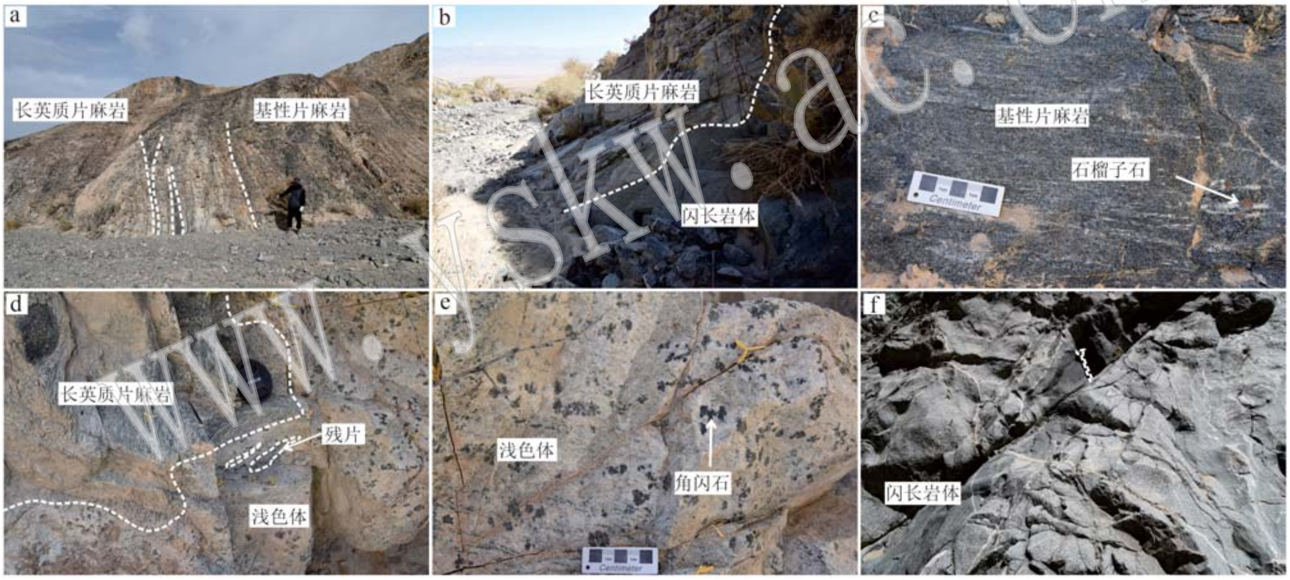

图 2　柴北缘拐角梁-双口山弧岩浆-变质单元岩石样品野外照片

Fig. 2　Field views of studied rock samples of Guaijiaoliang-Shuangkoushan arc-related rock unit, North Qaidam

a—长英质片麻岩与基性片麻岩野外关系; b—长英质片麻岩与闪长岩野外关系; c—含石榴子石基性片麻岩; d—长英质片麻岩与其浅色体的野外关系; e—浅色体中残留的角闪石; f—闪长岩野外露头

a—field relationship between felsic gneiss and basic gneiss; b—field relationship between felsic gneiss and diorite; c—basic gneiss with garnets; d—field relationship between felsic gneiss and leucosome; e—residual hornblende in leucosome; f—outcrop of diorite

长英质片麻岩由斜长石(50%~60%)、石英(20%~30%)、角闪石(10%~15%)及少量石榴子石和黑云母组成(图 3b),其内部的浅色体主要由斜长石(40%~50%)、石英(30%~35%)及角闪石(10%~15%)组成,其中斜长石与角闪石均以半自形产出(图 3c~3e)。

闪长岩中由斜长石(50%~60%)、角闪石(20%~30%)、石英(约 5%)及少量绿帘石组成(约 5%)(图 3f)。其中角闪石呈自形棱状,具备对顶双晶结构,斜长石则表面多蚀变为白云母。

3　测试方法

3.1　锆石 U-Pb 年代学

锆石颗粒通过常规分离方法制备后嵌入环氧树脂,并抛光以露出中心区域。为分析锆石形态特征、

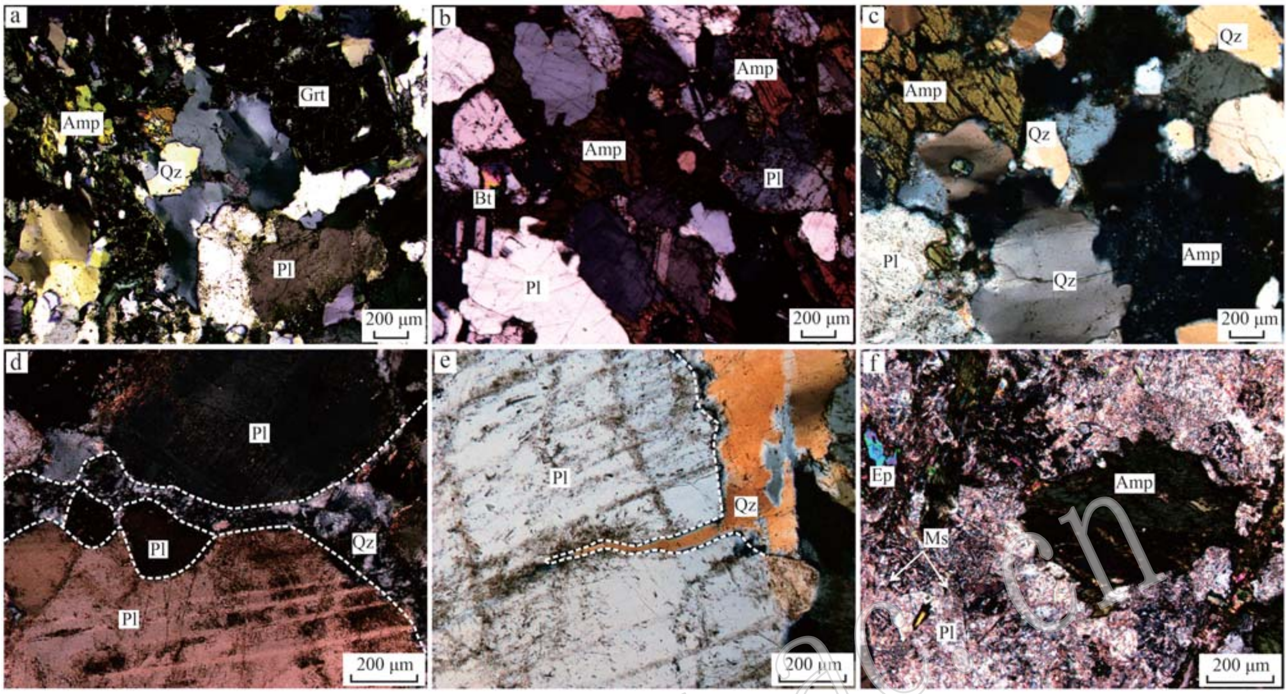

图 3 柴北缘拐角梁-双口山弧岩浆-变质单元岩石样品镜下照片(正交偏光)

Fig. 3 Photomicrographs of studied rock samples of Guaijiaoliang-Shuangkoushan arc-related rock unit, North Qaidam (crossed nicols)

a—基性片麻岩; b—长英质片麻岩; c—浅色体; d—浅色体的斜长石颗粒间发育长英质脉; e—浅色体中细长尖锐的石英颗粒沿斜长石的裂隙贯入; f—闪长岩; Grt—石榴子石; Amp—角闪石; Pl—斜长石; Qz—石英; Bt—黑云母; Ep—绿帘石; Ms—白云母

a—basic gneiss; b—felsic gneiss; c—leucosome; d—plagioclase grains in the leucosome develop felsic veins; e—elongated and sharp quartz particles in leucosome penetrate along the cracks of plagioclase; f—diorite; Grt—garnet; Amp—amphibole; Pl—plagioclase; Qz—quartz; Bt—biotite; Ep—epidote; Ms—muscovite

内部结构和确定测试点,进行了透射光、反射光及阴极发光成像。锆石 U-Pb 年代测定使用河北地质大学的 LA-MC-ICP-MS 进行,以氦气作为载气以增强剥蚀材料的传输效率。激光烧蚀光斑直径为 32 μm,其他分析步骤见侯可军等(2009)。以锆石 GJ-1 为外标,对样品锆石每 5 次分析后对 GJ-1 进行 2 次校准。依据 GJ-1 变化,每 5 次分析用线性插值法校正 U-Th-Pb 同位素比值的时变漂移。使用 Plešovice 作为控制标准,获得其加权平均 $^{206}Pb/^{238}U$ 年龄为 337±1 Ma,与推荐的 337.13±0.37 Ma 年龄一致。年龄计算与谐和图绘制均通过 Excel 宏程序 Isoplot 3.0 完成。

3.2 锆石 Lu-Hf 同位素分析

在完成锆石的 U-Pb 年龄测试后,对其进行 Lu-Hf 同位素分析,分析点位尽可能与 U-Pb 测试点位一致,从而保证获得锆石的 U-Pb 年龄和 Lu-Hf 同位素基本对应,避免不同分析位置的差异造成年龄和 Lu-Hf 同位素的不一致性。。锆石 Lu-Hf 同位素分析在河北地质大学完成,使用 Neptune 多接收器 ICP-MS 及 Newwave UP213 激光剥蚀系统,氦气作为载气,激光烧蚀直径 44 μm,详细步骤见侯可军等(2007)。设定 $^{176}Lu/^{175}Lu = 0.026\,58$ 和 $^{176}Yb/^{173}Yb = 0.796\,218$,以校正 ^{176}Lu 和 ^{176}Yb 对 ^{176}Hf 的谱峰干扰(Chu *et al.*, 2002)。为校正仪器质量偏差,Yb 同位素比值标准化为 $^{172}Yb/^{173}Yb = 1.352\,74$(Chu *et al.*, 2002)。使用指数法将 Hf 同位素比值标准化为 $^{179}Hf/^{177}Hf = 0.732\,5$。分析过程中,使用锆石标准 GJ-1 作为参考,得到其 $^{176}Hf/^{177}Hf$ 值为 0.282 007±8 (2σ),与推荐值在分析误差范围内一致(Elhlou *et al.*, 2006)。$\varepsilon Hf(t)$ 值的计算基于锆石的 U-Pb 年龄和球粒陨石的基准值: $^{176}Lu/^{177}Hf = 0.033\,2$, $^{176}Hf/^{177}Hf = 0.282\,77$(Blichert-Toft and Albarède, 1997)。单阶段模式年龄 t_{DM} 基于亏损地幔值: $^{176}Hf/^{177}Hf = 0.283\,25$, $^{176}Lu/^{177}Hf = 0.038\,4$(Griffin *et al.*, 2000),并使用 ^{176}Lu 衰变常数 1.867×10^{-11}/a (Söderlund *et al.*, 2004)。二阶段模式年龄 t_{DM}^{C} 基于平均大陆地壳的$^{176}Hf/^{177}Hf$ 值 0.015 计算(Griffin *et al.*, 2002)。

3.3 全岩主、微量元素分析

全岩的主量和微量元素分析在中国地质科学院完成,测试方法为 X 射线荧光光谱法(XRF)和电感耦合等离子体质谱(ICP-MS)。主量元素含量通过 XRF 法测定,含量大于 1 %的主量元素测试精度为 ±1%~3%,而含量小于 1 %的主量元素测试精度为 ±10%左右。微量和稀土元素分析通过 ICP-MS 完成,精度监控使用国际标准样品 BCR-1、BHVO-1、AGV-2 和 JB-1。基于对标准样品的重复分析,绝大多数微量元素的测试精度优于 5%。稀土元素通过阳离子交换技术分离,含量低于 10×10^{-6} 的稀土元素分析不确定性在 10%以内,含量高于 10×10^{-6} 的稀土元素分析不确定性在 5%以内。

4 测试结果

4.1 锆石 U-Pb 定年

基性片麻岩(21LLS8-1)、长英质片麻岩中的浅色体(21LLS5-1)以及闪长岩(21LLS4-1)这 3 个样品的锆石 U-Pb 年代学分析结果见表 1。

基性片麻岩样品的锆石呈自形短柱状,长度为 100~150 μm,长宽比约 2∶1,整体发光较弱,具有不明显的核-边结构,核部发光稍强,具有明显的振荡环带特征,为岩浆成因;边部具有明显的带状结构,属于典型的变质成因锆石(吴元保等, 2004)。选取核部 5 个测点测试,获取的$^{206}Pb/^{238}U$ 年龄为 473~470 Ma,加权平均年龄为 470.9 ± 6.5 Ma(MSWD = 0.019;图 4a),Th/U 值较高,为 0.025~0.186。锆石边部共分析了 20 个测点,$^{206}Pb/^{238}U$ 年龄为 436~418 Ma,加权平均值为 432.6 ± 4.0 Ma(MSWD = 0.37;图 4a),且 Th/U 值较低(0.001~0.118)。

长英质片麻岩中浅色体中的锆石呈自形短柱状,长度为 100~150 μm,长宽比约 3∶1,锆石整体发光较弱,具有核-幔-边结构,其中核部发光较弱,呈无分带或带状结构,属于典型的变质锆石;幔部发光最高,由于其分布较狭窄,暂无法通过结构区分其类型;边部呈现弱的振荡环带特征,代表其可能为深熔或岩浆成因锆石。选择测试锆石边部 17 个点位,获取$^{206}Pb/^{238}U$ 年龄为 445~440 Ma,加权平均年龄为 441.6±3.5 Ma(MSWD = 0.19;图 4b),Th/U 值低至 0.031~1.084。

闪长岩中的锆石呈现自形粒状,颗粒直径约 100 μm,锆石总体较为均一,主体部分呈弱发光,外部存在不均匀分布的高发亮窄边。样品中的锆石具有明显的振荡环带特征,为岩浆成因,共选取 27 个测点分析,$^{206}Pb/^{238}U$ 年龄为 449~436 Ma,其加权平均值为 441.6 ± 3.0 Ma(MSWD = 0.20;图 4c),Th/U 值为 0.273~0.631。

4.2 锆石 Lu-Hf 同位素

锆石 Lu-Hf 同位素分析结果见表 2。

基性片麻岩的$^{176}Hf/^{177}Hf$ 值介于 0.282 693~0.282 811 之间,相应的 $\varepsilon Hf(t)$ 值变化于+6.74~+11.26 之间。在 $\varepsilon Hf(t)-t$ 图中,数据点可明确分为两组:一组为锆石核部数据,一组为锆石边部数据。其中锆石核部年龄相对应的 $\varepsilon Hf(t)$ 值介于+10.46~+11.36 之间,锆石边部年龄相对应的 $\varepsilon Hf(t)$ 值则介于+6.74~+10.95 之间(图 5)。浅色体的$^{176}Hf/^{177}Hf$ 值介于 0.282 749~0.282 859 之间,相应的 $\varepsilon Hf(t)$ 值变化于+7.24~+12.27 之间。在 $\varepsilon Hf(t)-t$ 图中,所有数据点都位于亏损地幔演化线之下(图 5)。闪长岩的$^{176}Hf/^{177}Hf$ 值介于 0.282 645~0.282 731 之间,相应的 $\varepsilon Hf(t)$ 值变化于+5.13 ~ +8.06 之间(图 5)。

4.3 全岩地球化学

本文对基性片麻岩(21LLS8-6、21LLS8-8)、长英质片麻岩(21LLS6-7、21LLS7-4)及其中的浅色体(21LLS5-3、21LLS5-5)以及闪长岩(21LLS4-2、21LLS4-4)4 组样品开展了全岩主量和微量元素分析,结果见表 3。

基性片麻岩 SiO_2(52.16%~53.69%)、Al_2O_3(15.41%~15.51%)和 K_2O(0.37%~0.28%)含量较低,而 FeO^T(10.03%~10.16%)、MgO(5.71%~6.99%)、CaO(7.60%~8.26%)及 Na_2O(2.49%~2.95%)含量相对较高,$Mg^{\#}$ 值为 36.28~40.75,在 TAS 图解中,样品落于辉长闪长岩区域,在 K_2O-SiO_2 图解中,样品落于低钾拉斑系列范围(图 6),基性片麻岩微量元素显示出富集 LILEs 而亏损 HFSEs 的特征(图 7a),稀土元素呈现略为右倾的平坦的稀土元素配分模式,$(La/Yb)_N$ = 2.41~3.20,无明显 Eu 异常特征(Eu/Eu^* = 0.93~1.01;图 7b)。

长英质片麻岩 SiO_2(70.32%~71.06%)和 Na_2O(3.74%~3.99%)含量较高,而 Al_2O_3(13.62%~13.89%)、FeO^T(3.24%~4.87%)、MgO(1.04%~2.04%)、CaO(3.06%~3.81%)和 K_2O(0.11%~

表 1 鱼卡地区闪长岩、浅色体、基性片麻岩锆石 U-Pb 年代分析结果

Table 1 Zircon U-Pb analyzed data for the diorite, leucosomes and basic gneiss in the Yuka area

测点号	$w_B/10^{-6}$		Th/U	同位素比值						同位素年龄/Ma					
	Th	U		$^{207}Pb/^{206}Pb$	1σ	$^{207}Pb/^{235}U$	1σ	$^{206}Pb/^{238}U$	1σ	$^{207}Pb/^{206}Pb$	1σ	$^{207}Pb/^{235}U$	1σ	$^{206}Pb/^{238}U$	1σ
21LLS4-1 闪长岩															
1	170	367	0.463	0.055 3	0.000 8	0.538 7	0.012 6	0.070 6	0.001 5	433	30	438	8	440	9
2	199	443	0.448	0.055 6	0.000 8	0.542 5	0.011 8	0.070 7	0.001 3	435	30	440	8	440	8
3	172	394	0.437	0.055 4	0.000 8	0.548 4	0.011 7	0.071 7	0.001 2	428	33	444	8	446	7
4	174	303	0.574	0.055 4	0.000 8	0.536 6	0.011 4	0.070 2	0.001 3	428	30	436	8	437	8
5	51.5	126	0.409	0.055 9	0.002 0	0.541 5	0.025 1	0.070 5	0.002 3	450	80	439	17	439	14
6	139	390	0.357	0.054 5	0.000 9	0.539 8	0.013 5	0.071 7	0.001 3	391	37	438	9	446	8
7	413	680	0.607	0.055 1	0.000 7	0.547 3	0.011 8	0.071 9	0.001 3	417	26	443	8	448	8
8	354	706	0.501	0.057 0	0.001 1	0.557 6	0.014 4	0.071 2	0.001 7	500	72	450	9	443	10
9	207	513	0.403	0.055 3	0.000 6	0.547 3	0.011 5	0.071 8	0.001 3	433	28	443	8	447	8
10	176	388	0.454	0.056 5	0.000 8	0.553 0	0.012 8	0.070 8	0.001 3	472	31	447	8	441	8
11	229	573	0.401	0.055 3	0.000 7	0.542 7	0.011 6	0.071 1	0.001 3	433	26	440	8	443	8
12	144	228	0.631	0.055 0	0.001 0	0.547 1	0.012 8	0.072 1	0.001 3	413	41	443	8	449	8
13	122	229	0.533	0.055 6	0.001 1	0.544 2	0.013 4	0.071 0	0.001 2	439	43	441	9	442	7
14	232	533	0.435	0.054 7	0.000 8	0.537 0	0.012 3	0.071 2	0.001 5	467	33	436	8	443	9
15	173	332	0.521	0.056 1	0.000 7	0.548 2	0.011 2	0.070 7	0.001 3	457	28	444	7	441	8
16	112	315	0.357	0.056 6	0.001 0	0.551 4	0.013 8	0.070 6	0.001 5	476	42	446	9	440	9
17	64.9	112	0.579	0.056 8	0.002 7	0.544 7	0.018 8	0.071 1	0.001 7	483	106	442	12	443	10
18	69.0	124	0.559	0.055 4	0.002 0	0.540 8	0.017 9	0.071 4	0.001 6	428	80	439	12	445	9
19	157	349	0.450	0.055 9	0.000 9	0.549 2	0.012 2	0.071 3	0.001 4	456	33	444	8	444	8
20	69.9	148	0.471	0.055 7	0.001 4	0.543 9	0.016 1	0.070 7	0.001 2	443	56	441	11	440	7
21	74.3	148	0.502	0.055 5	0.001 4	0.539 3	0.016 8	0.070 3	0.001 3	435	62	438	11	438	8
22	107	198	0.543	0.056 8	0.001 0	0.551 8	0.013 7	0.070 2	0.001 1	483	41	446	9	438	6
23	44.8	164	0.273	0.052 9	0.001 4	0.515 6	0.014 7	0.070 8	0.001 1	328	59	422	10	441	6
24	48.7	96.4	0.505	0.057 3	0.001 4	0.559 1	0.016 0	0.071 0	0.001 4	502	56	451	10	442	8
25	155	371	0.419	0.056 6	0.001 2	0.556 6	0.021 3	0.070 9	0.001 5	472	46	449	14	441	9
26	229	450	0.508	0.060 0	0.001 0	0.580 1	0.015 8	0.070 0	0.001 2	611	37	465	10	436	7
27	84.3	163	0.519	0.056 1	0.001 0	0.543 7	0.012 5	0.070 2	0.001 0	457	41	441	8	437	6
21LLS5-1 浅色体															
1	29.5	441	0.067	0.057 3	0.000 8	0.564 1	0.016 3	0.071 4	0.001 8	502	30	454	11	445	11
2	408	423	0.963	0.057 1	0.001 0	0.557 6	0.018 3	0.070 7	0.001 7	494	73	450	12	440	10
3	17.6	490	0.036	0.055 9	0.000 8	0.550 6	0.011 8	0.071 3	0.001 2	456	31	445	8	444	7
4	192	342	0.561	0.057 5	0.001 2	0.564 7	0.013 6	0.071 2	0.000 9	509	44	455	9	443	6
5	299	317	0.942	0.058 6	0.001 7	0.566 2	0.019 6	0.069 8	0.000 8	554	58	456	13	435	5
6	504	465	1.084	0.056 9	0.000 7	0.558 8	0.012 8	0.071 1	0.001 3	487	31	451	8	443	8

续表 1

Continued Table 1

测点号	$w_B/10^{-6}$		Th/U	同位素比值						同位素年龄/Ma					
	Th	U		$^{207}Pb/^{206}Pb$	1σ	$^{207}Pb/^{235}U$	1σ	$^{206}Pb/^{238}U$	1σ	$^{207}Pb/^{206}Pb$	1σ	$^{207}Pb/^{235}U$	1σ	$^{206}Pb/^{238}U$	1σ
7	288	319	0.905	0.056 7	0.001 3	0.553 9	0.015 6	0.070 7	0.000 8	480	52	448	10	440	5
8	475	608	0.781	0.056 7	0.000 6	0.558 6	0.010 9	0.071 4	0.001 2	480	26	451	7	445	7
9	74.1	549	0.135	0.056 6	0.000 8	0.556 9	0.013 8	0.071 2	0.001 3	476	25	449	9	443	8
10	128	239	0.536	0.057 0	0.001 8	0.550 9	0.012 5	0.071 2	0.001 6	500	73	446	8	443	10
11	164	231	0.710	0.056 8	0.000 9	0.559 3	0.013 0	0.071 4	0.001 3	483	31	451	8	445	8
12	44.8	218	0.206	0.054 9	0.001 3	0.532 7	0.011 6	0.070 9	0.001 4	409	56	434	8	442	9
13	16.7	443	0.038	0.056 6	0.001 5	0.554 8	0.012 3	0.071 1	0.000 9	476	92	448	8	443	6
14	41.1	613	0.067	0.058 5	0.001 3	0.570 3	0.017 4	0.071 0	0.001 8	550	48	458	11	442	11
15	375	447	0.839	0.057 5	0.000 7	0.563 3	0.011 0	0.071 0	0.001 3	509	58	454	7	442	8
16	35.9	115	0.314	0.056 4	0.001 3	0.553 0	0.019 2	0.071 1	0.001 9	465	52	447	13	443	11
17	8.94	286	0.031	0.055 2	0.001 0	0.541 1	0.012 6	0.071 5	0.001 6	420	36	439	8	445	10
21LLS8-1 基性片麻岩															
1	15.5	1037	0.015	0.056 1	0.000 9	0.538 9	0.016 4	0.069 7	0.001 9	457	40	438	11	435	11
2	19.4	972	0.020	0.056 3	0.001 2	0.539 7	0.016 4	0.069 8	0.001 8	461	46	438	11	435	11
3	17.8	709	0.025	0.057 0	0.001 7	0.596 3	0.019 5	0.076 1	0.001 4	500	60	475	12	473	8
4	12.4	105	0.118	0.055 4	0.002 3	0.533 3	0.026 4	0.069 9	0.001 9	432	88	434	18	436	11
5	1.30	228	0.006	0.056 6	0.002 2	0.542 6	0.022 4	0.069 8	0.001 6	480	85	440	15	435	10
6	16.0	890	0.018	0.056 5	0.002 4	0.540 0	0.023 4	0.069 7	0.001 5	472	94	438	15	434	9
7	59.2	318	0.186	0.055 9	0.002 3	0.579 8	0.022 3	0.075 7	0.001 7	450	123	464	14	470	10
8	9.99	623	0.016	0.056 9	0.002 1	0.546 2	0.023 5	0.069 7	0.001 5	500	81	443	15	434	9
9	8.80	768	0.011	0.056 8	0.001 5	0.544 7	0.015 4	0.069 7	0.001 1	483	53	442	10	435	6
10	0.69	181	0.004	0.056 9	0.001 7	0.543 8	0.014 9	0.069 8	0.001 4	487	65	441	10	435	8
11	4.87	529	0.009	0.056 0	0.000 7	0.540 9	0.022 3	0.069 9	0.002 7	454	26	439	15	435	16
12	2.25	427	0.005	0.056 8	0.000 7	0.594 5	0.011 6	0.075 9	0.001 2	483	34	474	7	471	7
13	0.85	163	0.005	0.056 2	0.001 0	0.540 2	0.012 2	0.069 8	0.001 2	457	41	439	8	435	7
14	13.0	626	0.021	0.053 8	0.001 7	0.539 0	0.019 5	0.069 8	0.002 4	365	66	438	13	435	15
15	1.20	197	0.006	0.056 3	0.002 4	0.544 4	0.032 8	0.069 8	0.002 0	465	99	441	22	435	12
16	0.69	486	0.001	0.056 3	0.000 6	0.542 2	0.011 3	0.069 9	0.001 4	465	24	440	7	435	8
17	11.5	931	0.012	0.056 3	0.000 6	0.539 9	0.014 3	0.069 6	0.001 8	465	22	438	9	434	11
18	16.8	1184	0.014	0.055 8	0.000 6	0.536 6	0.016 0	0.069 6	0.001 9	456	29	436	11	434	12
19	10.9	847	0.013	0.056 0	0.000 6	0.540 1	0.013 3	0.069 8	0.001 5	454	24	439	9	435	9
20	18.9	917	0.021	0.056 4	0.000 5	0.542 7	0.012 7	0.069 6	0.001 5	478	25	440	8	434	9
21	0.46	168	0.003	0.057 5	0.001 2	0.531 9	0.013 2	0.067 0	0.001 0	509	51	433	9	418	6
22	15.6	978	0.016	0.056 0	0.000 7	0.538 8	0.012 8	0.069 8	0.001 7	450	21	438	8	435	10
23	0.77	413	0.002	0.056 5	0.001 0	0.590 7	0.012 1	0.075 7	0.000 9	472	37	471	8	470	6
24	12.9	821	0.016	0.056 9	0.000 7	0.595 1	0.013 5	0.075 6	0.001 3	487	31	474	9	470	8
25	0.47	282	0.002	0.055 9	0.000 9	0.536 8	0.012 7	0.069 6	0.001 4	450	37	436	8	434	8

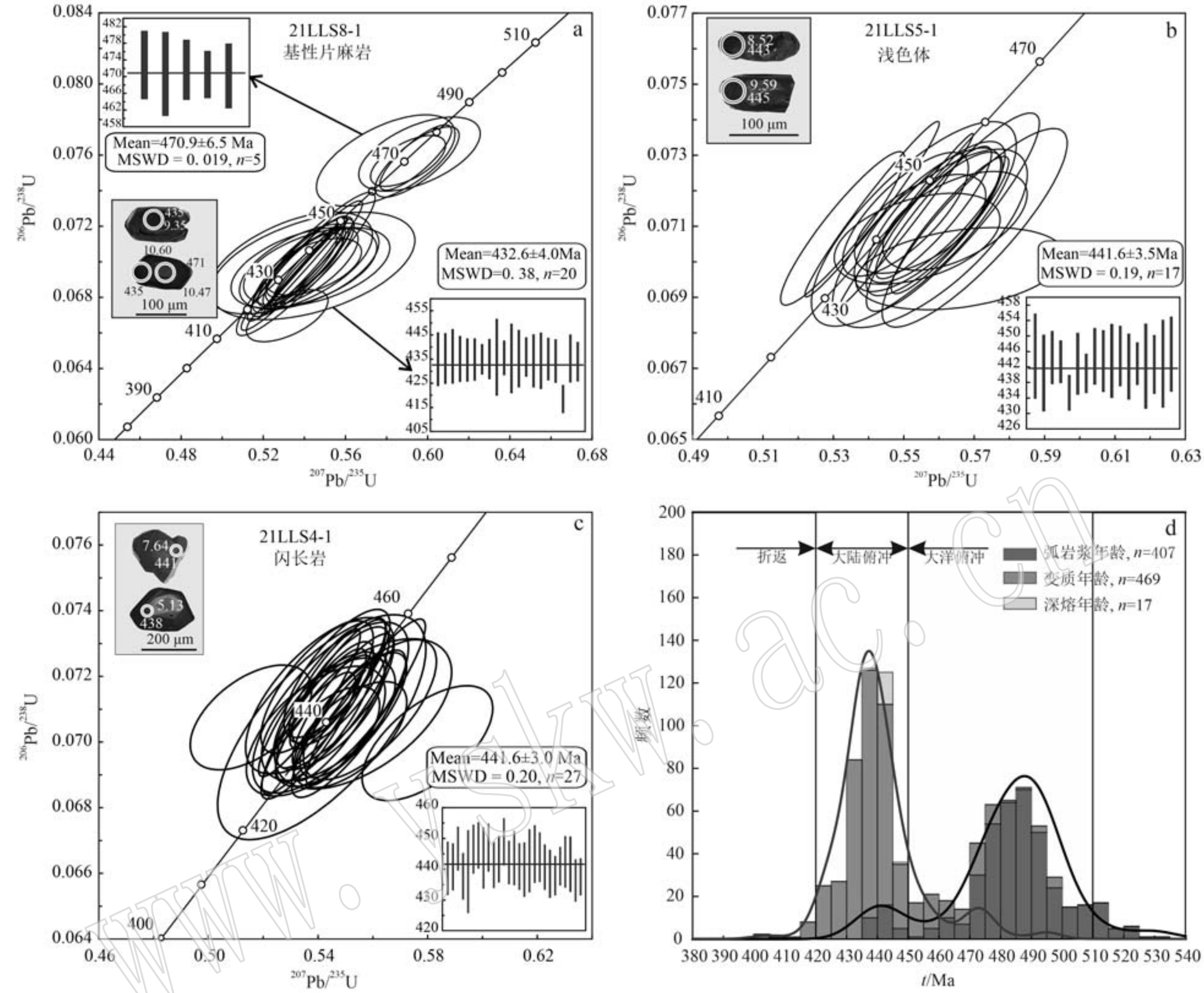

图4 柴北缘拐角梁-双口山弧岩浆-变质单元岩石样品U-Pb年龄谐和图(a~c)和频率分布直方图(d)

Fig. 4 U-Pb concordia diagram for rock samples of Guaijiaoliang-Shuangkoushan arc-related rock unit, North Qaidam (a~c) and frequency dustribution histograms(d)

图4d中数据来源：弧岩浆年龄(史仁灯等, 2004; 朱小辉等, 2014; Wang *et al.*, 2018; Li *et al.*, 2018, 2022; Yu *et al.*, 2019a, 2019c; Gao *et al.*, 2021; Cai *et al.*, 2021)；变质年龄(马旭东等, 2006; Chen *et al.*, 2007; Zhang *et al.*, 2008a, 2010, 2011, 2017; Yu *et al.*, 2015c, 2019a, 2019c; Ren *et al.*, 2017, 2019; Wang *et al.*, 2018; Yang *et al.*, 2020; Cai *et al.*, 2021)

data source in Fig. 4d: arc magma age (Shi Rendeng *et al.*, 2004; Zhu Xiaohui *et al.*, 2014; Wang *et al.*, 2018; Li *et al.*, 2018, 2022; Yu *et al.*, 2019a, 2019c; Cai *et al.*, 2021; Gao *et al.*, 2021; metamorphic age (Ma Xudong *et al.*, 2006; Chen *et al.*, 2007; Zhang *et al.*, 2008a, 2010, 2011, 2017; Yu *et al.*, 2015c, 2019a, 2019c; Ren *et al.*, 2017, 2019; Wang *et al.*, 2018; Yang *et al.*, 2020; Cai *et al.*, 2021)

0.44%)含量较低(图6),铝饱和指数为1.03~1.12,属于弱过铝质岩石,$Mg^{\#}$值为17.60~38.63。在TAS图解中,样品落于花岗闪长岩区域,在K_2O-SiO_2图解中,样品落于低钾拉斑系列范围(图6)。长英质片麻岩显示出与基性片麻岩类近似的微量元素特征,同样富集LILEs而亏损HFSEs(图7a),而具有略微右倾的稀土元素配分模式,$(La/Yb)_N=3.63\sim5.38$,其中LREEs展现出右倾趋势$(La/Sm)_N=2.5\sim2.6$,HREEs则表现出相对更为平坦的配分模式,$(Gd/Lu)_N=1.1\sim1.2$,Eu表现出微弱的负异常($Eu/Eu^*=0.85\sim0.87$; 图7b)。

浅色体的SiO_2含量为71.17 %~71.19%,具有相对较低的Al_2O_3(13.95%~14.22 %)、FeO^T(2.51%~2.59%)、MgO(0.94%~0.97%)、CaO(3.64%~3.79%)和K_2O(0.21%~0.23%)含量以及相对较高的Na_2O(5.15%~5.18%)含量,铝饱和指数为0.91~0.94,指示其属于准铝质岩石,样品在TAS图解中落于花岗闪长岩区域(图6)。

表 2　鱼卡地区闪长岩、浅色体、基性片麻岩锆石 Hf 同位素数据

Table 2　Zircon Hf isotopic data of the diorite, leucosomes and basic gneiss in the Yuka area

测点号	t/Ma	^{176}Yb/^{177}Hf	2σ	^{176}Lu/^{177}Hf	2σ	^{176}Hf/^{177}Hf	2σ	^{176}Hf/^{177}Hf$_t$	εHf(t)	t_{DM}/Ma	t_{DM}^{C}/Ma	f_s
21LLS4-1 闪长岩												
1	442	0.010 297	0.000 035	0.000 424	0.000 001	0.282 676	0.000 019	0.282 673	6.22	803	943	−0.987 235
2	442	0.015 866	0.000 032	0.000 618	0.000 001	0.282 699	0.000 019	0.282 693	6.96	776	903	−0.981 400
3	442	0.009 117	0.000 031	0.000 374	0.000 002	0.282 710	0.000 020	0.282 707	7.44	755	877	−0.988 738
4	442	0.022 654	0.000 381	0.000 776	0.000 013	0.282 701	0.000 016	0.282 695	7.01	775	900	−0.976 620
5	442	0.024 216	0.000 451	0.000 863	0.000 015	0.282 720	0.000 020	0.282 712	7.63	751	866	−0.974 011
6	442	0.011 187	0.000 094	0.000 459	0.000 003	0.282 680	0.000 018	0.282 676	6.33	799	937	−0.986 167
7	442	0.009 686	0.000 017	0.000 398	0.000 000	0.282 671	0.000 018	0.282 668	6.06	810	952	−0.988 021
8	442	0.009 207	0.000 043	0.000 382	0.000 001	0.282 674	0.000 021	0.282 671	6.16	805	946	−0.988 507
9	442	0.009 358	0.000 061	0.000 375	0.000 001	0.282 645	0.000 018	0.282 642	5.13	846	1002	−0.988 692
10	442	0.020 433	0.000 099	0.000 679	0.000 002	0.282 687	0.000 019	0.282 681	6.53	794	926	−0.979 553
11	442	0.022 383	0.000 039	0.000 741	0.000 002	0.282 731	0.000 018	0.282 725	8.06	733	842	−0.977 682
12	442	0.011 623	0.000 046	0.000 490	0.000 003	0.282 677	0.000 017	0.282 673	6.23	804	942	−0.985 238
13	442	0.007 232	0.000 017	0.000 288	0.000 000	0.282 697	0.000 017	0.282 695	7.00	771	900	−0.991 324
14	442	0.034 521	0.000 039	0.001 230	0.000 004	0.282 667	0.000 020	0.282 657	5.66	834	973	−0.962 946
15	442	0.033 491	0.000 092	0.001 067	0.000 001	0.282 697	0.000 019	0.282 688	6.76	788	913	−0.967 870
16	442	0.012 534	0.000 024	0.000 475	0.000 001	0.282 695	0.000 018	0.282 692	6.89	778	906	−0.985 687
17	442	0.007 667	0.000 011	0.000 284	0.000 000	0.282 692	0.000 018	0.282 689	6.81	779	911	−0.991 454
18	442	0.020 840	0.000 894	0.000 720	0.000 029	0.282 696	0.000 018	0.282 690	6.83	782	910	−0.978 322
19	442	0.009 430	0.000 132	0.000 374	0.000 004	0.282 716	0.000 016	0.282 713	7.64	747	865	−0.988 722
20	442	0.009 591	0.000 033	0.000 353	0.000 001	0.282 671	0.000 017	0.282 668	6.05	809	952	−0.989 367
21	442	0.026 932	0.000 276	0.000 880	0.000 007	0.282 725	0.000 017	0.282 718	7.81	744	856	−0.973 500
22	442	0.010 826	0.000 057	0.000 444	0.000 003	0.282 723	0.000 017	0.282 719	7.87	739	853	−0.986 616
23	442	0.008 864	0.000 014	0.000 357	0.000 001	0.282 712	0.000 019	0.282 709	7.50	753	873	−0.989 260
24	442	0.013 151	0.000 076	0.000 443	0.000 002	0.282 680	0.000 018	0.282 676	6.35	798	936	−0.986 660
25	442	0.010 348	0.000 014	0.000 429	0.000 001	0.282 684	0.000 018	0.282 680	6.49	793	928	−0.987 081
26	442	0.010 541	0.000 101	0.000 433	0.000 003	0.282 675	0.000 016	0.282 671	6.16	806	946	−0.986 973
27	442	0.012 490	0.000 072	0.000 512	0.000 002	0.282 703	0.000 017	0.282 699	7.14	768	893	−0.984 593
28	442	0.006 677	0.000 019	0.000 267	0.000 000	0.282 718	0.000 019	0.282 716	7.74	742	860	−0.991 943
21LLS5-1 长英质片麻岩中浅色体												
1	443	0.013 078	0.000 165	0.000 612	0.000 006	0.282 749	0.000 016	0.282 744	8.75	706	806	−0.981 578
2	443	0.031 096	0.001 331	0.001 107	0.000 042	0.282 776	0.000 014	0.282 767	9.59	676	760	−0.966 664
3	443	0.074 286	0.001 904	0.002 909	0.000 053	0.282 773	0.000 023	0.282 749	8.95	715	795	−0.912 379
4	443	0.070 771	0.004 657	0.002 352	0.000 152	0.282 790	0.000 019	0.282 770	9.70	680	754	−0.929 165
5	443	0.085 972	0.002 165	0.002 828	0.000 070	0.282 813	0.000 018	0.282 789	10.36	655	718	−0.914 812
6	443	0.050 491	0.002 358	0.001 698	0.000 058	0.282 772	0.000 016	0.282 758	9.25	694	779	−0.948 861
7	443	0.057 486	0.000 552	0.001 951	0.000 017	0.282 760	0.000 019	0.282 744	8.78	715	804	−0.941 230
8	443	0.021 901	0.000 125	0.000 853	0.000 005	0.282 773	0.000 016	0.282 766	9.56	676	762	−0.974 313
9	443	0.117 814	0.003 292	0.003 787	0.000 100	0.282 841	0.000 022	0.282 810	11.10	629	678	−0.885 930
10	443	0.044 580	0.002 530	0.001 540	0.000 079	0.282 762	0.000 018	0.282 749	8.94	705	796	−0.953 614
11	443	0.069 702	0.002 262	0.002 356	0.000 065	0.282 809	0.000 018	0.282 789	10.38	651	717	−0.929 044
12	443	0.027 634	0.000 215	0.001 046	0.000 006	0.282 784	0.000 014	0.282 775	9.88	664	744	−0.968 509
13	443	0.054 863	0.007 618	0.001 863	0.000 222	0.282 777	0.000 018	0.282 761	9.39	689	771	−0.943 896
14	443	0.026 699	0.001 868	0.001 063	0.000 071	0.282 797	0.000 015	0.282 788	10.34	646	719	−0.967 972
15	443	0.217 454	0.002 244	0.006 793	0.000 058	0.282 757	0.000 024	0.282 701	7.24	829	888	−0.795 391
16	443	0.055 075	0.003 293	0.001 946	0.000 108	0.282 859	0.000 019	0.282 843	12.27	571	614	−0.941 371
17	443	0.041 636	0.001 354	0.001 603	0.000 057	0.282 772	0.000 019	0.282 759	9.29	691	776	−0.951 715
18	443	0.111 258	0.003 154	0.003 610	0.000 090	0.282 778	0.000 016	0.282 748	8.92	721	796	−0.891 265
19	443	0.069 627	0.000 807	0.002 298	0.000 021	0.282 756	0.000 016	0.282 737	8.52	728	818	−0.930 778
20	443	0.076 936	0.003 564	0.002 722	0.000 107	0.282 859	0.000 020	0.282 836	12.04	584	626	−0.918 013
21	443	0.043 161	0.000 296	0.001 681	0.000 009	0.282 857	0.000 017	0.282 843	12.26	571	614	−0.949 364

续表 2

Continued Table 2

测点号	t/Ma	$^{176}Yb/^{177}Hf$	2σ	$^{176}Lu/^{177}Hf$	2σ	$^{176}Hf/^{177}Hf$	2σ	$^{176}Hf/^{177}Hf_t$	$\varepsilon Hf(t)$	t_{DM}/Ma	t_{DM}^{C}/Ma	f_s
21LLS8-1 基性片麻岩												
1	435	0.005 736	0.000 123	0.000 229	0.000 004	0.282 791	0.000 022	0.282 789	10.18	641	721	−0.993 093
2	435	0.003 762	0.000 072	0.000 143	0.000 003	0.282 763	0.000 017	0.282 762	9.22	678	774	−0.995 704
3	435	0.001 654	0.000 037	0.000 055	0.000 001	0.282 805	0.000 015	0.282 804	10.73	618	692	−0.998 358
4	471	0.006 949	0.000 046	0.000 271	0.000 002	0.282 777	0.000 019	0.282 774	10.47	661	735	−0.991 837
5	435	0.004 818	0.000 106	0.000 190	0.000 004	0.282 693	0.000 016	0.282 692	6.74	775	909	−0.994 277
6	435	0.005 915	0.000 232	0.000 234	0.000 010	0.282 796	0.000 020	0.282 794	10.36	634	712	−0.992 943
7	435	0.003 805	0.000 047	0.000 141	0.000 002	0.282 749	0.000 017	0.282 748	8.73	697	801	−0.995 754
8	435	0.002 408	0.000 062	0.000 085	0.000 002	0.282 811	0.000 019	0.282 811	10.95	610	680	−0.997 433
9	435	0.003 357	0.000 085	0.000 128	0.000 003	0.282 718	0.000 015	0.282 717	7.63	740	860	−0.996 137
10	435	0.004 594	0.000 043	0.000 180	0.000 002	0.282 796	0.000 016	0.282 795	10.38	632	710	−0.994 578
11	435	0.001 838	0.000 009	0.000 066	0.000 001	0.282 801	0.000 017	0.282 801	10.60	623	699	−0.998 006
12	435	0.002 764	0.000 039	0.000 106	0.000 001	0.282 768	0.000 016	0.282 767	9.42	670	763	−0.996 821
13	435	0.004 859	0.000 019	0.000 182	0.000 000	0.282 765	0.000 017	0.282 763	9.28	675	770	−0.994 522
14	435	0.005 290	0.000 125	0.000 200	0.000 005	0.282 757	0.000 017	0.282 755	8.99	687	786	−0.993 962
15	435	0.003 368	0.000 094	0.000 126	0.000 004	0.282 766	0.000 016	0.282 765	9.32	674	768	−0.996 201
16	435	0.005 251	0.000 109	0.000 205	0.000 005	0.282 746	0.000 017	0.282 744	8.61	702	807	−0.993 811
17	435	0.001 842	0.000 033	0.000 067	0.000 002	0.282 778	0.000 017	0.282 777	9.77	656	744	−0.997 992
18	471	0.005 129	0.000 036	0.000 192	0.000 002	0.282 784	0.000 016	0.282 782	10.75	649	720	−0.994 218
19	471	0.006 441	0.000 154	0.000 254	0.000 006	0.282 778	0.000 018	0.282 776	10.53	658	731	−0.992 336
20	435	0.003 363	0.000 058	0.000 127	0.000 002	0.282 734	0.000 014	0.282 733	8.22	717	829	−0.996 176
21	471	0.005 345	0.000 023	0.000 209	0.000 001	0.282 776	0.000 018	0.282 774	10.46	660	735	−0.993 711
22	435	0.003 732	0.000 027	0.000 136	0.000 001	0.282 805	0.000 017	0.282 804	10.70	620	693	−0.995 894
23	435	0.003 029	0.000 038	0.000 119	0.000 002	0.282 780	0.000 016	0.282 779	9.82	654	741	−0.996 411
24	435	0.001 401	0.000 005	0.000 046	0.000 000	0.282 781	0.000 019	0.282 780	9.87	652	738	−0.998 600
25	471	0.004 263	0.000 064	0.000 152	0.000 002	0.282 798	0.000 017	0.282 797	11.26	629	692	−0.995 433
26	435	0.003 217	0.000 008	0.000 119	0.000 001	0.282 773	0.000 018	0.282 772	9.59	663	754	−0.996 409
27	435	0.002 502	0.000 030	0.000 088	0.000 002	0.282 766	0.000 015	0.282 765	9.35	672	767	−0.997 360

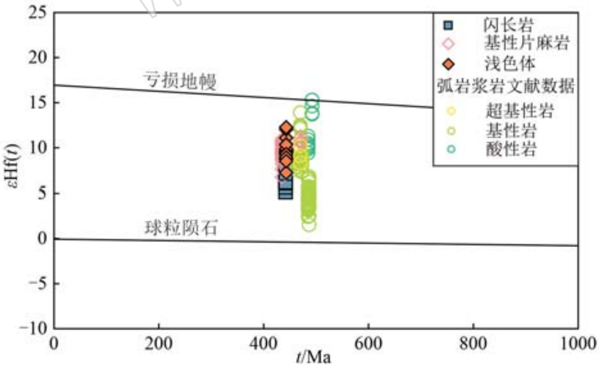

图 5 柴北缘拐角梁-双口山弧岩浆-变质单元岩石 Lu-Hf 同位素示意图

Fig. 5 Diagram of Lu-Hf isotope rocks of Guaijiaoliang-Shuangkoushan arc-related rock unit, North Qaidam

数据来源：超基性岩(Yu *et al.*, 2019c)；基性岩(袁桂邦等, 2002；史仁灯等, 2004；Yu *et al.*, 2019a, 2019c；Gao *et al.*, 2021；Li *et al.*, 2022)；酸性岩(Wu *et al.*, 2006；朱小辉等, 2014)

data source: ultrobasic rocks (Yu *et al.*, 2019c); basic rocks (Yuan Guibang *et al.*, 2002; Shi Rendeng *et al.*, 2004; Yu *et al.*, 2019a, 2019c; ; Gao *et al.*, 2021; Li *et al.*, 2022); acid rocks (Wu *et al.*, 2006; Zhu Xiaohui *et al.*, 2014)

浅色体微量元素特征与长英质片麻岩类似，即 LILEs 显著富集而 HFSEs 明显亏损(图 7a)，但具有更加右倾的稀土元素配分模式，$(La/Yb)_N=7.84\sim7.85$，其中 LREEs 具右倾趋势，$(La/Sm)_N=3.1\sim3.2$，HREEs 则具相对更为平坦的配分模式，$(Gd/Lu)_N=1.1\sim1.2$，且具微弱的 Eu 负异常($Eu/Eu^*=0.79\sim0.85$；图 7b)。

闪长岩的 SiO_2 含量为 52.78%～54.02%，具有较高的 CaO(7.93%～8.00%)、Al_2O_3(19.00%～19.46%)、Na_2O(4.01%～4.05%)和 K_2O(1.00%～1.13%)含量以及较低的 FeO^T(6.81%～7.17%)和 MgO(3.51%～3.59%)含量(图 6)，$Mg^\#$值为 33.35～34.00，铝饱和指数为 0.88～0.90，属于准铝质岩石。在 TAS 图解中，样品落于辉长闪长岩区域，在 K_2O-SiO_2 图解中，样品落于钙碱性系列范围(图 6)。闪长岩与上述 3 类样品具有相似的微量元素分布特征，富集LILEs而亏损HFSEs(图7c)，稀土元素表现出

表 3　鱼卡地区闪长岩、长英质片麻岩、浅色体、基性片麻岩主量元素(w_B/%)和微量元素($w_B/10^{-6}$)含量

Table 3　Contents of major elements (w_B/%) and trace elements ($w_B/10^{-6}$) of the diorite, felsic gneiss, leucosomes and basic gneiss in the Yuka area

岩性	闪长岩		长英质片麻岩		浅色体		基性片麻岩	
样品编号	21LLS4-2	21LLS4-4	21LLS6-7	21LLS7-4	21LLS5-3	21LLS5-5	21LLS8-6	21LLS8-8
SiO_2	52.78	54.02	71.06	70.32	71.19	71.17	52.16	53.69
Al_2O_3	19.46	19.00	13.62	13.89	14.22	13.95	15.41	15.51
$Fe_2O_3^T$	7.97	7.57	5.41	3.60	2.79	2.88	11.29	11.14
FeO^T	7.17	6.81	4.87	3.24	2.51	2.59	10.16	10.03
MgO	3.59	3.51	1.04	2.04	0.94	0.97	6.99	5.71
CaO	7.93	8.00	3.06	3.81	3.64	3.79	8.26	7.60
Na_2O	4.05	4.01	3.99	3.74	5.18	5.15	2.49	2.95
K_2O	1.13	1.00	0.11	0.44	0.23	0.21	0.37	0.28
MnO	0.15	0.15	0.15	0.05	0.05	0.06	0.14	0.17
TiO_2	0.70	0.55	0.24	0.34	0.38	0.35	0.87	0.83
P_2O_5	0.26	0.24	0.02	0.05	0.11	0.10	0.09	0.10
LOI	1.66	1.62	0.94	1.40	0.88	1.00	1.62	1.70
Total	99.68	99.67	99.64	99.68	99.60	99.62	99.69	99.69
$Mg^{\#}$	33.35	34.00	17.60	38.63	27.24	27.23	40.75	36.28
A/CNK	0.90	0.88	1.12	1.03	0.94	0.91	0.80	0.83
A/NK	2.47	2.47	2.04	2.10	1.62	1.60	3.43	3.01
FC3MS	0.70	0.66	1.55	0.76	0.65	0.64	0.83	1.00
Sc	18.09	17.91	13.98	17.49	10.20	9.86	37.06	35.66
V	169.63	179.11	21.40	57.16	56.67	56.73	265.70	262.89
Cr	5.72	6.03	1.76	38.96	2.62	1.65	57.70	53.95
Co	20.49	20.56	4.11	7.56	4.65	4.58	33.65	29.12
Ni	9.05	8.27	1.11	12.76	3.14	3.44	30.08	27.00
Cu	92.00	113.18	3.10	6.71	5.87	3.28	15.62	21.86
Zn	85.06	89.13	10.55	28.99	13.08	15.16	82.60	57.65
Ga	20.92	20.88	9.59	14.28	11.85	11.86	18.22	18.08
Rb	24.19	27.95	4.05	21.00	5.97	6.16	11.27	6.98
Sr	1 151.29	1 185.55	323.29	408.00	277.53	266.64	326.81	449.82
Y	16.69	18.67	32.64	23.54	18.14	17.84	22.72	23.17
Zr	71.09	96.41	108.51	116.83	114.59	102.22	59.12	62.50
Nb	3.29	4.90	1.50	2.99	3.00	3.19	2.77	1.75
Cs	1.86	1.99	2.85	4.31	1.33	1.29	2.87	2.17
Ba	593.96	695.13	116.69	869.88	199.61	177.87	133.42	119.63
La	32.69	35.60	9.78	13.56	16.30	15.90	5.32	8.31
Ce	61.29	68.87	24.37	30.42	32.37	31.64	17.00	19.69
Pr	7.34	8.49	2.66	3.83	4.24	4.15	2.67	2.75
Nd	28.78	34.67	11.39	16.23	17.11	17.47	13.39	12.87
Sm	4.24	5.58	2.41	3.54	3.34	3.24	3.38	3.12
Eu	1.28	1.57	0.81	0.97	0.84	0.84	1.06	1.11
Gd	3.67	4.62	3.39	3.47	3.16	2.81	3.62	3.56
Tb	0.50	0.63	0.68	0.61	0.51	0.49	0.61	0.65
Dy	2.93	3.27	4.66	3.77	2.87	2.97	3.79	3.97
Ho	0.56	0.69	1.02	0.83	0.67	0.63	0.81	0.89
Er	1.57	2.02	2.97	2.48	1.97	2.04	2.40	2.62
Tm	0.25	0.30	0.44	0.36	0.31	0.29	0.34	0.38
Yb	1.74	1.84	2.69	2.52	2.08	2.03	2.21	2.60
Lu	0.24	0.27	0.38	0.37	0.33	0.31	0.33	0.42
Hf	2.26	2.72	3.21	3.48	3.40	3.17	1.89	2.01
Ta	0.18	0.23	0.09	0.16	0.13	0.20	0.15	0.11
Pb	10.63	10.55	2.34	3.14	2.46	2.16	2.38	2.72
Th	8.19	8.57	2.83	3.32	3.51	3.54	0.52	1.87
U	0.54	0.78	0.25	0.30	0.30	0.42	0.31	0.35
Sr/Y	68.99	63.49	9.90	17.33	15.30	14.95	14.39	19.41
$(La/Yb)_N$	18.73	19.37	3.63	5.38	7.85	7.84	2.41	3.20
$(Nb/Yb)_N$	1.88	2.66	0.56	1.18	1.44	1.57	1.26	0.67
Eu/Eu^*	0.99	0.95	0.87	0.85	0.79	0.85	0.93	1.01

$FC3MS = FeO^T/CaO - 3(MgO/SiO_2)$。

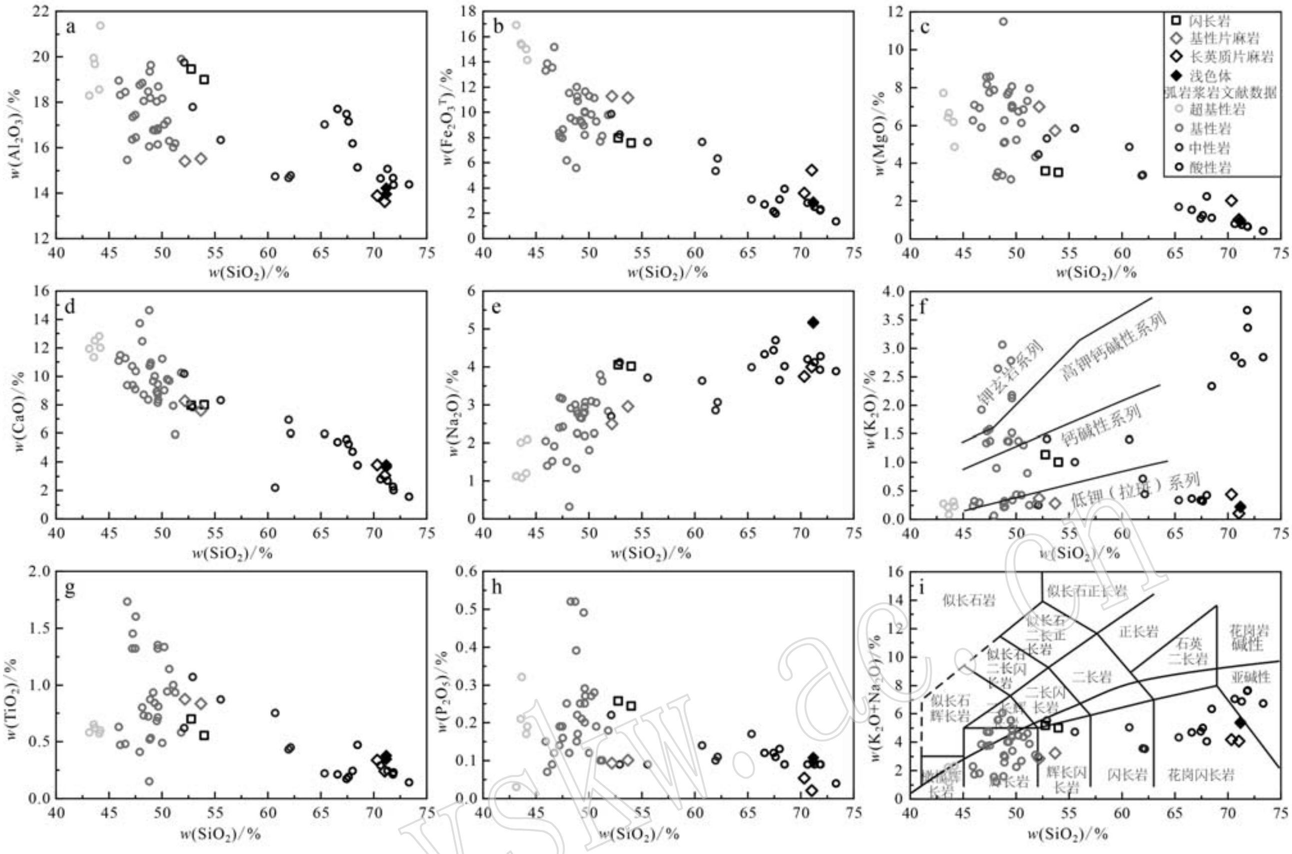

图 6 柴北缘拐角梁-双口山弧岩浆-变质单元岩石主量元素哈克图解(a~h)和 TAS 图解(i,据 Middlemost, 1994)

Fig. 6 Harker diagrams of major elements (a~h) and TAS diagram (i, after Middlemost, 1994) of Guaijiaoliang-Shuangkoushan arc-related rock unit, North Qaidam

数据来源：超基性岩(Yu *et al.*, 2019c)；基性岩(袁桂邦等, 2002; 史仁灯等, 2004; Yu *et al.*, 2019a, 2019c; Gao *et al.*, 2021; Li *et al.*, 2022)；中性岩(史仁灯等, 2004; Wu *et al.*, 2006; Yu *et al.*, 2019c)；酸性岩(Wu *et al.*, 2006; 朱小辉等, 2014)

data source: ultrabasic rocks (Yu *et al.*, 2019c); basic rocks (Yuan Guibang *et al.*, 2002; Shi Rendeng *et al.*, 2004; Yu *et al.*, 2019a, 2019c; Gao *et al.*, 2021; Li *et al.*, 2022); intermediate rock (Shi Rendeng *et al.*, 2004; Wu *et al.*, 2006; Yu *et al.*, 2019c); acid rocks (Wu *et al.*, 2006; Zhu Xiaohui *et al.*, 2014)

显著的右倾配分模式,$(La/Yb)_N = 18.73\sim19.37$,无明显 Eu 异常特征($Eu/Eu^* = 0.95\sim0.99$; 图 7d)。

5 讨论

5.1 岩浆和深熔作用时代

基性片麻岩锆石核部具有明显的振荡环带特征,Th 和 U 含量较高,Th/U = 0.002~0.186,为典型的岩浆锆石(图 4a)。定年结果显示基性片麻岩原岩年龄为 470.9 ± 6.5 Ma,表明其形成于洋壳俯冲阶段(王振强等, 2022)。闪长岩锆石颗粒总体较为均一,发育明显的振荡环带,锆石加权平均年龄为 441.6 ± 3.0 Ma,对应于陆壳俯冲阶段。基性片麻岩锆石边部具有明显的带状结构(Th/U = 0.001~0.118,图 4a),与典型变质成因锆石特征一致(吴元保等, 2004),加权平均年龄为 432.6 ± 4.0 Ma; 浅色体的锆石边部具有 441.6±3.5 Ma 的加权平均年龄,具有现弱的振荡环带结构(图 4b),类似于深熔成因锆石(Zheng *et al.*, 2006),这两组年龄或对应陆壳俯冲过程中的一期变质-深熔事件。

依据前人的文献数据及本文定年工作,可将柴北缘俯冲碰撞杂岩带奥陶系-志留系岩浆-深熔活动划分为两个期次(图 4d): ① 约 470 Ma 洋壳俯冲阶段,柴北缘发育广泛的弧岩浆活动,形成包含弧火山岩、变辉长岩、基性高压麻粒岩、长英质片麻岩的原岩及闪长岩为主的大陆弧杂岩,分布于都兰、乌兰等地区(史仁灯等, 2004; 朱小辉等, 2014; Li *et al.*, 2018, 2022; Wang *et al.*, 2018; Yu *et al.*, 2019a, 2019c; Cai *et al.*, 2021; Gao *et al.*, 2021); ② 约 440 Ma 陆壳俯冲阶段, 伴随普遍的岩浆-深熔活动,

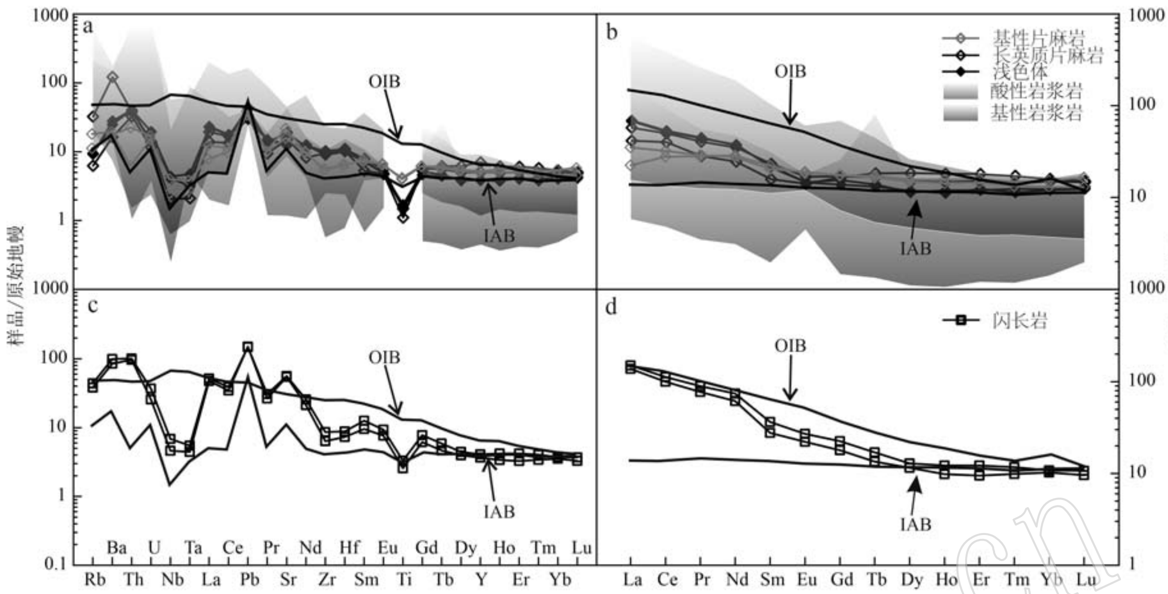

图 7　柴北缘拐角梁-双口山弧岩浆-变质单元岩石原始地幔归一化蛛蛛图(a、c、e)和球粒陨石归一化稀土元素图(b、d、f)(球粒陨石和原始地幔归一化值来自 Sun and McDonough, 1989)

Fig. 7　Primitive mantle-normalized spidergram (a, c, e) and chondrite-normalized rare earth element pattern (b, d, f) of rock samples in Guaijiaoliang-Shuangkoushan arc-related rock unit, North Qaidam (chondrite and primitive mantle-normalized values are from Sun and McDonough, 1989)

形成包括分布于锡铁山、都兰及团鱼山等地区的S型花岗岩、埃达克质浅色体以及闪长岩等(Wu *et al*., 2009; Zhao *et al*., 2017; Yu *et al*., 2019c)。

5.2　弧岩浆成因

除了地幔源区属性和熔融程度,鱼卡地区拐角梁-双口山弧岩浆-变质单元内基性片麻岩、长英质片麻岩及闪长岩的地球化学组成还可能取决于诸如分离结晶、地壳混染等一系列岩浆过程,因此,在分析岩石成因与反演地幔源区之前必须评估以上综合因素的影响。在岩浆侵位过程中,分离结晶作用会对岩浆成分产生显著影响(庞阿娟等, 2012)。拐角梁-双口山弧岩浆-变质单元内基性片麻岩的 MgO 与其他主量元素氧化物含量的关系如图 8。Ca 在单斜辉石中是相容的而 Al 则正好相反,因此,单斜辉石的结晶造成了残余熔体中 MgO 与 CaO/Al_2O_3 值呈现正相关关系(Hill *et al*., 2011)(图 8a)。MgO 与 Na_2O 之间的负相关关系(图 8e)以及不存在明显的负 Eu 异常(图 7b)说明斜长石并没有作为结晶分异相离开岩浆系统。样品 Sr/Y(14.3~19.4)和 Y/Yb(8.9~10.3)值变化范围相对较小,且轻重稀土元素的分异不明显,表明分离结晶并非为基性片麻岩原岩的主要成因。

根据样品的微量元素和同位素特征,可以判别拐角梁-双口山弧岩浆-变质单元内基性片麻岩的原岩在岩浆侵位过程中是否经历了地壳物质的混染。在壳幔分异过程中,不相容元素趋向富集于长英质大陆地壳。对于研究的样品,Nb/La 值与 SiO_2 含量并没有表现出正相关关系,这与混染大陆地壳物质所表现的趋势不一致(图 8j)。Nb、U 具有相同的地球化学行为,其比值在部分熔融和岩浆分异过程中趋向于一致,因此,这一属性可以用来判别陆壳混染是否影响了原本封闭的岩浆体系(Hofmann and Jochum, 1996)。鱼卡地区拐角梁-双口山基性片麻岩样品具有与幔源岩浆一致的高 Nb/U 值,加之 Nb/U 值与样品 SiO_2 含量之间并不存在负相关关系(图 8i),指示拐角梁-双口山基性片麻岩样品在岩浆侵位过程中并未经历陆壳混染作用。另外,这些样品的锆石具一致的形态学特征,且锆石 Hf 同位素变化很小,结合一致的锆石 U-Pb 年龄和微量元素特征(图 7a),也说明陆壳混染发生的可能性很低。

鱼卡地区拐角梁-双口山弧岩浆-变质单元内基性片麻岩具有较高的 MgO 含量及较低的 SiO_2 含量,指示了源自地幔的超镁铁质部分熔融作用。同

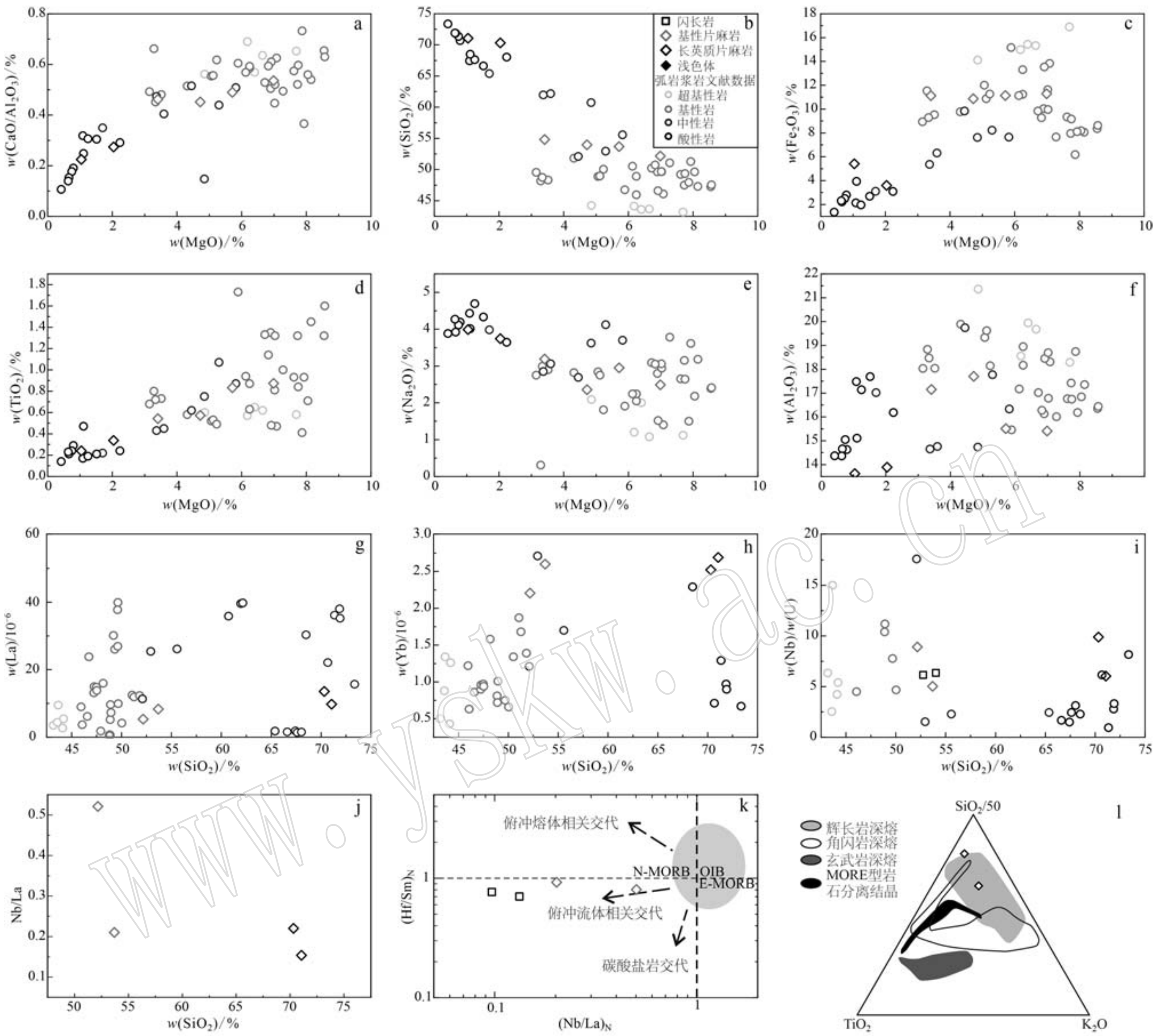

图8 柴北缘拐角梁-双口山弧岩浆-变质单元岩石主量元素-MgO哈克图解(a~f)、微量元素-SiO_2哈克图解(g~j)、$(Hf/Sm)_N$-$(Nb/La)_N$图解(k,据 LaFlèche *et al.*, 1998)和SiO_2-TiO_2-K_2O三元图解(l,参考数据源自 France *et al.*, 2010)

Fig. 8 The major elements-MgO Harker diagrams (a~f), Harker diagrams of trace elements-SiO_2(g~h), $(Hf/Sm)_N$-$(Nb/La)_N$ diagram (k, after LaFlèche *et al.*, 1998) and SiO_2-TiO_2-K_2O diagram (l, comparable data from France *et al.*, 2010) of rocks in Guaijiaoliang-Shuangkoushan arc-related rock unit, North Qaidam

数据来源:超基性岩(Yu *et al.*, 2019c);基性岩(袁桂邦等, 2002;史仁灯等, 2004;Yu *et al.*, 2019a, 2019c;Gao *et al.*, 2021;Li *et al.*, 2022);中性岩(史仁灯等, 2004;Wu *et al.*, 2006;Yu *et al.*, 2019c);酸性岩(Wu *et al.*, 2006;朱小辉等, 2014)

Data source: ultrabasic rocks (Yu *et al.*, 2019c); basic rocks (Yuan Guibang *et al.*, 2002; Shi Rendeng *et al.*, 2004; Yu *et al.*, 2019a, 2019c; Gao *et al.*, 2021; Li *et al.*, 2022); intermediate rock (Shi Rendeng *et al.*, 2004; Wu *et al.*, 2006; Yu *et al.*, 2019c); acid rocks (Wu *et al.*, 2006; Zhu Xiaohui *et al.*, 2014)

时,这些样品呈现出富集大离子亲石元素和轻稀土元素(如Cs、Ba、K和Sr)、亏损高场强元素(如Nb、Zr)的特征,并且具有Ti、Ta、Nb的弧形微量元素模式,进一步暗示了其与俯冲带流体交代的地幔楔密切相关(Kelemen *et al.*, 2014;Hernández-Uribe *et al.*, 2021;Li *et al.*, 2022)。鉴于柴北缘俯冲碰撞杂岩带的形成时代背景,其地球化学特征的成因可能存在以下两种:岩浆经历同化混染地壳物质,

或是俯冲过程中洋壳物质与地幔楔橄榄岩的源区发生混合。如图 8k 所示，鱼卡地区拐角梁-双口山弧岩浆-变质单元内基性片麻岩具有较低的 $(Nb/La)_N$ 值和中等的 $(Hf/Sm)_N$ 值，且表现出流体端员混合趋势。结合镜下所见其矿物组合中角闪石、绿帘石等富水矿物的存在（图 3a），我们认为鱼卡基性片麻岩的原岩形成于地幔源区，且该区域受到来自俯冲洋壳富水流体的交代作用。

La-SiO_2 和 Yb-SiO_2 体系是判别长英质片麻岩的原岩来源于部分熔融或分离结晶的两个重要参数（Brophy, 2008, 2009）：基于数值模拟和理论计算，对于基性或者中性角闪岩发生部分熔融形成的长英质片麻岩，随着长英质熔体中 SiO_2 含量的升高，与原岩相比，熔体中 La、Yb 含量几乎不变或者稍下降，进而导致稀土元素总量与原岩基性岩中的稀土元素总量相近似。而与此相反的结晶分异作用主导产生的长英质片麻岩，随着长英质熔体中 SiO_2 含量的不断升高，其中的 La 和 Yb 含量也会随之增长（图 8g、8h），并且长英质片麻岩稀土元素总量明显高于初始母岩浆中的稀土元素总量。长英质片麻岩样品 $[(La/Yb)_N=2.6\sim3.9]$ 表现出相较于基性片麻岩样品 $[(La/Yb)_N=1.7\sim2.3]$ 更为亏损的重稀土元素组成进一步证明了我们的推测（Taylor, 1967; Rudnick and Gao, 2003; Davidson and Arculus, 2006）。本研究中长英质片麻岩与其伴生基性片麻岩的稀土元素含量特征符合结晶分异趋势（图 7b）。根据实验岩石学证据，辉长岩深熔成因的长英质片麻岩的 TiO_2 含量要明显低于结晶分异或熔体不混溶成因的长英质片麻岩的 TiO_2 含量（Berndt *et al.*, 2004; Koepke *et al.*, 2004, 2005, 2007; Furnes and Dilek, 2017）。鱼卡地区拐角梁-双口山地区长英质片麻岩的 TiO_2 含量高于 MORB 结晶分异实验所得长英质片麻岩的 TiO_2 含量（图 6g），与结晶分异所形成的长英质熔体中 TiO_2 含量相对应，暗示长英质片麻岩的分离结晶成因。此外，在 $TiO_2-K_2O-SiO_2/50$ 三端员图解上（France *et al.*, 2010），长英质片麻岩样品也落在结晶分异的实验熔体范围内（图 8l）。基于基性片麻岩与长英质片麻岩之间明显的互层关系、一致的成岩年龄、区域上持续的幔源岩浆活动，长英质片麻岩最有可能来源于同时期基性片麻岩岩浆的结晶分异，长英质片麻岩与基性片麻岩具有相似的锆石 Hf 同位素组成（王秉璋等, 2022; 图 5），暗示两者来自同一个地幔源区（成分、同位素组成相似）。

闪长岩可能起源于幔源镁铁质岩浆的结晶分异、含水地幔的部分熔融以及壳-幔岩浆混合作用（Annen *et al.*, 2006; Bachmann and Huber, 2016）。地幔来源的中-基性岩浆通常表现出同位素组成上的亏损或轻微富集特征，因此，来自幔源岩浆的分离结晶产物，理论上应具有相应的地幔型同位素特征。然而，在本研究中，虽然闪长岩呈现出地幔型同位素组成特征，但其成因并非源自幔源岩浆的结晶分异过程。据数值模拟，原始幔源玄武质岩浆如果通过岩浆分异产生熔体，需要经历至少 60%~70%结晶分异（Annen *et al.*, 2006）。闪长岩若通过基性岩浆结晶分异形成，则会产生与之伴生的大体量镁铁质堆晶岩。然而，野外地质表明并没有大体量的、成分上与闪长岩互补的基性堆积体出现，排除了样品源于基性岩浆结晶分异的可能性。镜下鉴定未发现针状磷灰石和斜长石反环带结构的存在，且锆石 Hf 同位素组成范围相对较窄（图 5），排除了岩浆混合的可能性。不少研究提出具地幔型同位素特征的闪长岩来源于俯冲下插的洋壳在角闪岩相条件下的部分熔融（Niu and O'Hara, 2009; Niu *et al.*, 2013; Song *et al.*, 2015）。一方面，俯冲洋壳在角闪岩相条件下部分熔融是基于俯冲带高地热梯度下的暖-热俯冲（Niu *et al.*, 2013; 唐跃等, 2021）；另一方面，柴北缘在古生代存在多期地壳深熔事件以及野外广泛出露的混合岩化证据（Li *et al.*, 2018; Yu *et al.*, 2012, 2015a, 2019b, 2019c）。鱼卡地区拐角梁-双口山弧岩浆-变质单元内闪长岩熔体显示出明显高于 0.65 的 FC3MS 值，Nb/Ta 值（18.1~24.9）与幔源岩浆相近（17.5±2.0; Jochum *et al.*, 1989），且远高于下地壳（8.3; Rudnick and Gao, 2003），进一步暗示熔体来源于地幔的部分熔融（Yang and Zhou, 2013; Yang *et al.*, 2016），样品较低的 $Mg^{\#}$ 值特征，也与地幔来源熔体相一致（Herzberg, 2006; Sobolev *et al.*, 2007）。

俯冲大洋板片交代地幔，具有比 MORB 源区更加富集的放射性同位素组成，呈现低的 Nb/U 值（Hofmann *et al.*, 1986; Jackson *et al.*, 2007）。本研究样品闪长岩富集大离子亲石元素（如 Rb、Th、Ba），亏损高场强元素（如 Nb、Ta、Zr、Hf 和 Ti），具中等的 $(Nb/La)_N$ 和 $(Hf/Sm)_N$ 值（图 8k），与含水地幔部分熔融过程中流体交代作用有关，角闪石等含水矿物的大量存在表明熔融过程中有水的参与。因此，我们倾向于认为鱼卡地区拐角梁-双口山弧岩浆-变质单元

内闪长岩来源于约440 Ma洋壳俯冲到陆-陆碰撞过程中软流圈上涌,含水地幔部分熔融形成闪长岩。

5.3 长英质片麻岩原岩的深熔作用

野外岩石学观察表明,拐角梁-双口山弧岩浆-变质单元内的长英质片麻岩经历了强烈的部分熔融,长英质片麻岩内的浅色体与寄主岩之间边界模糊,浅色体含量约30%且多以浅色脉体及浅色体布丁的形式产出(图2d~2e),代表先前的熔体迁移通道及熔体汇聚区,抑或是代表熔体萃取后的残余熔体。显微镜下晶粒结构的观察可以进一步推断长英质片麻岩是否受到深熔作用的影响,浅色体的斜长石颗粒间发育由斜长石+石英组成的显微细脉,可能为熔体迁移通道(Sawyer, 2008; Holness *et al.*, 2011; 图3d); 细长尖锐的石英颗粒沿斜长石的裂隙贯入(图3e),代表先前熔体的结晶(Yu *et al.*, 2015c)。这些微观矿物结构是深熔作用典型的镜下矿物学证据,代表了熔体生长和迁移过程(Chen *et al.*, 2013)。

浅色体与寄主长英质片岩之间无明确分界线,浅色体通道及汇聚区未见暗色体,且浅色体中均匀分布有大量转熔角闪石而无不含水的转熔矿物(如石榴子石、堇青石和辉石等),这与水致熔融现象一致(Brown, 2013; Weinberg and Hasalová, 2015)。浅色体的主量元素和微量元素组成可以用来揭示深熔过程,特别用于区分水致熔融和脱水熔融。不同的熔融机制造成主、微量元素和同位素特征的显著差异(Gao *et al.*, 2017)。Ab、An和Or的比例为区分水致熔融和脱水熔融产生的熔体成分提供了一个可靠的指标(Pichavant *et al.*, 1992; Patiño-Douce, 1996; Becker *et al.*, 1998; Weinberg and Hasalová, 2015)。在部分熔融过程中,熔融体系中加水会产生更多的英云闪长质到奥长花岗质的熔体(Patiño-Douce and Harris, 1998; Castro, 2013),而脱水熔融则会产生相对富钾的花岗质熔体(Patiño-Douce and Beard, 1995; Patiño-Douce and Harris, 1998; Patiño-Douce, 2005),本研究中的浅色体在An-Ab-Or图解中均落于奥长花岗岩区域(图9a),与水致熔融实验岩石学结果一致。

熔体中Rb、Sr、Ba的浓度主要受原岩云母和长石分解的控制,由于云母和长石可作为深熔反应的主要消耗物,且脱水熔融与水致熔融倾向于消耗不同比例的云母和长石,因而熔体中这些元素的差异可用于区分熔融机制(Inger and Harris, 1993; Watt and Harley, 1993; McDermott *et al.*, 1996; Zeng *et al.*, 2005)。一般来说,水致熔融过程中,会消耗相对更大比例的斜长石,从而产生具有高Sr、Ba和低Rb、Rb/Sr特征的熔体(Inger and Harris, 1993; Knesel and Davidson, 2002; Gao *et al.*, 2017),本研究的样品与这一趋势基本吻合(图9b、9c)。当前,对于通过熔体中Rb、Sr及Ba的相对含量判断熔融机制存在一定争论,有学者认为使用这些指标是不准确的,如Bartoli(2021)通过对纳米花岗岩的研究认为,熔体中的这些微量元素成分更多受控于原岩成分及压力变化,与流体关联性不大(图9b、9c)。尽管如此,我们还是可以通过结合其他微量元素指标的方式来共同判断长英质片麻岩的熔融特征,如浅色体与长英质片麻岩相比,并不存在脱水熔融导致熔体具有强烈Eu负异常的现象,且熔体中的Th与U的相对含量也满足水致熔融趋势(图9d; Gao *et al.*, 2017)。

综合野外调查、岩相学及主微量元素分析,我们认为拐角梁-双口山弧岩浆-变质单元中的长英质片麻岩经历了强烈的水致部分熔融,熔融反应或为:Bt + Pl + Qz + H_2O = Amp + Melt(Lappin and Hollister, 1980)。与之类似的熔融机制在北大别造山带中的罗田穹窿、岳西穹窿以及喀喇昆仑地区均有报道(Reichardt *et al.*, 2010),而依据转熔反应,大致可推测这类含角闪石的浅色体可能是长英质片麻岩在675~750℃和0.6~0.8 GPa条件下发生水致熔融形成的(Lappin and Hollister, 1980; Mclellan, 1988; Reichardt *et al.*, 2010),这与区内高角闪岩相变质记录基本吻合。一般变质岩发生水致熔融需要外部流体的加入(Yakymchuk *et al.*, 2019; Lee and Cho, 2020; Schorn *et al.*, 2021; Lee *et al.*, 2021),本区内同时期的闪长质岩浆侵位与结晶过程中释放的流体或是触发长英质片麻岩水致熔融关键因素。

5.4 对大陆地壳成熟的意义

俯冲带大陆地壳生长存在玄武岩模式和安山岩模式两种假说(Castro *et al.*, 2013)。其中,玄武岩模式需要通过拆沉多余镁铁质组分及经历岩浆混合或同化增加陆壳组分两个关键步骤,推动弧区陆壳的净生长(Jull and Kelemen, 2001; Lee *et al.*, 2007)。而安山岩模式则是安山质岩浆直接起源于洋壳和沉积物混合而成的岩浆源区,以此直接实现大陆壳的净生长(Kelemen *et al.*, 2003a, 2003b; Castro *et al.*, 2013; Tamura *et al.*, 2016)。

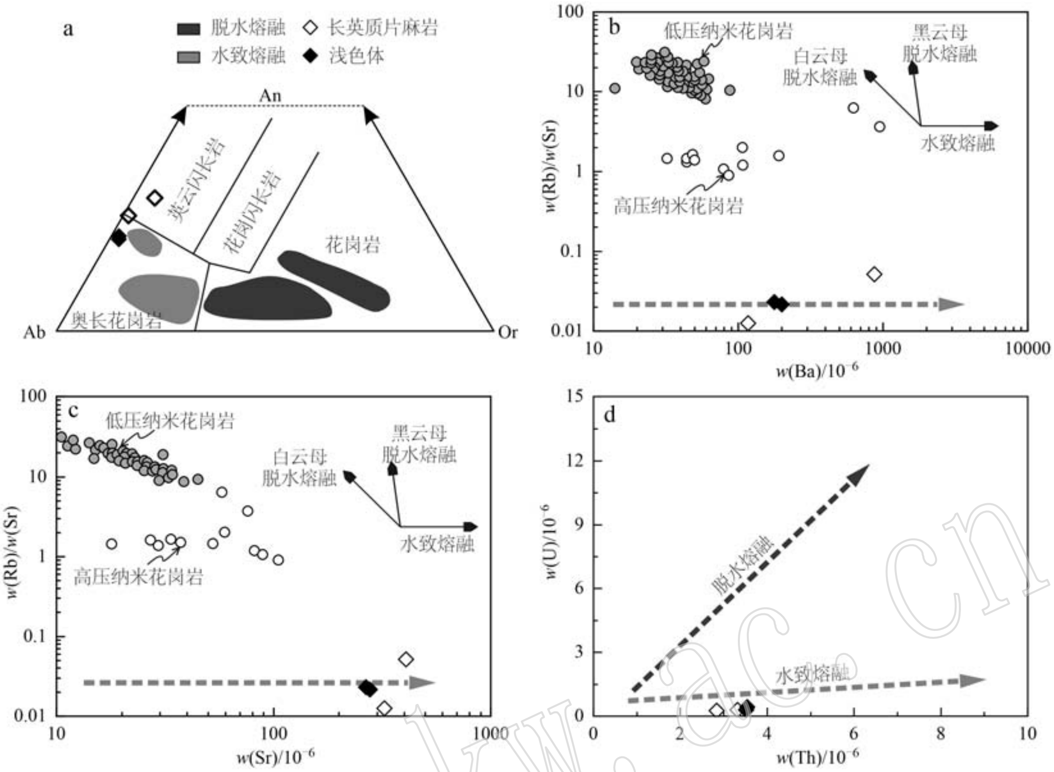

图 9　柴北缘拐角梁-双口山弧岩浆-变质单元长英质片麻岩和浅色体的 An-Ab-Or 三角图(a，据 Barker，1979)、Rb/Sr-Ba 图解(b，据 Inger and Harris，1993)、Rb/Sr-Sr 图解(c，据 Knesel and Davidson，2002)和 U-Th 图解(d，趋势线引自 Gao *et al.*，2017)

Fig. 9　An-Ab-Or diagram (a, after Barker), Rb/Sr-Ba diagram (b, after Inger and Harris, 1993), Rb/Sr-Sr diagram (c, after Knesel and Davidson, 2002) and U-Th diagram (d, trendlines after Gao *et al.*, 2017) showing the compositions of felsic gneisses and leucosomes of Guaijiaoliang-Shuangkoushan arc-related rock unit, North Qaidam

洋壳俯冲阶段，柴北缘俯冲碰撞杂岩带鲜有中-酸性弧岩浆的报道，仅在赛什腾及乌兰地区存在少量报道，但均被解释为来自古老或新生地壳的部分熔融(王秉璋等，2022；Gao *et al.*，2022，2023)。本文中所获取的长英质片麻岩与基性片麻岩之间存在明显的演化关系，均源于弧岩浆的结晶分异(见 5.2)，代表了约 470 Ma 的一次陆壳生长事件(图 10a)。该过程与新特提斯洋岩石圈俯冲形成冈底斯岩浆带并产生弧岩浆的过程相似，只不过冈底斯岩浆带在碰撞前弧岩浆分离结晶形成了丰富的富含角闪石的堆积物(如角闪石和角闪石辉长岩)(Zhu *et al.*，2022)。在陆-陆碰撞阶段，柴北缘俯冲碰撞杂岩带多数花岗岩类岩浆作用被认为是地壳重熔的结果，同样新特提斯洋板块在约 70 Ma 开始回卷，弧下地壳部分熔融形成长英质岩浆(Zhu *et al.*，2022)。与之不同的是，本文中约 440 Ma 的闪长岩则为陆壳俯冲阶段，软流圈上涌含水地幔部分熔融形成的，代表陆弧地壳的又一生长事件(图 10b)。

陆弧地壳向大陆地壳转化以完成大陆地壳的生长，需要经历不同程度的改造以达到与大陆地壳相同的成分(马超等，2019)。柴北缘俯冲碰撞杂岩带从洋壳俯冲到陆-陆碰撞均经历了强烈的地壳改造，其中洋壳俯冲阶段，乌兰与都兰地区分别记录了 465～450 Ma 及约 470 Ma 的地壳深熔事件(Li *et al.*，2018；Yu *et al.*，2019a)，反映大洋俯冲时期对陆弧地壳的改造。而陆-陆碰撞阶段的深熔事件主要集中在陆壳折返阶段(Sun *et al.*，2020；Yang *et al.*，2020)，主要以变基性岩和片麻岩的脱水熔融为主(Chen *et al.*，2012；Yu *et al.*，2015a，2015b，2019a，2019b；Cao *et al.*，2017)，而本文长英质片麻岩的水致部分熔融则发生于陆壳俯冲阶段，熔融机制和熔融时代明显区别于前者，反映了大陆板片俯冲与折返过程中不同的地壳改造机制。有意思的是，与都兰地体中同时代的变辉长岩在加厚下地壳

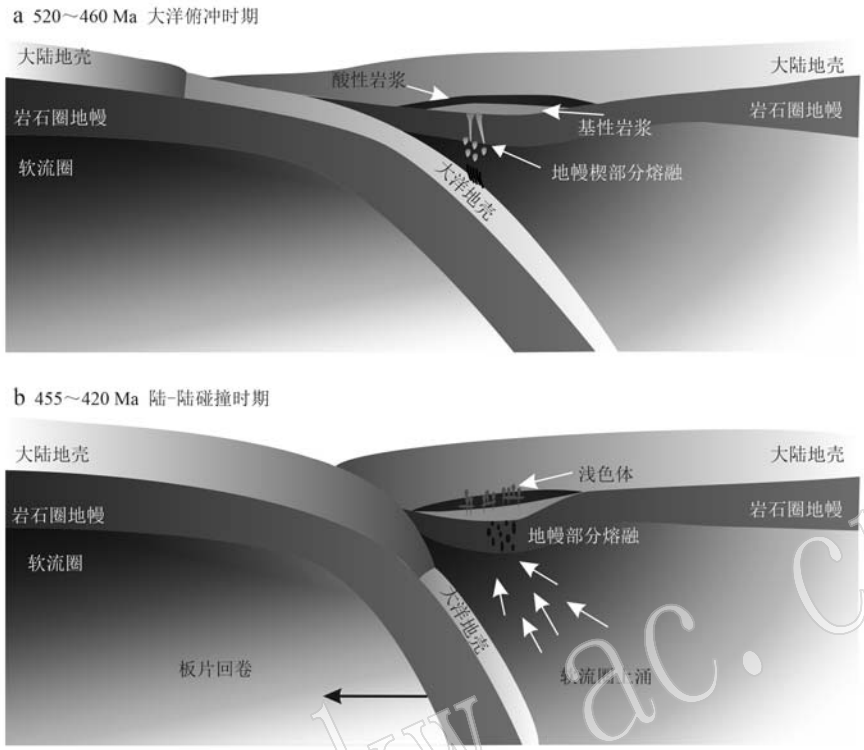

图 10 柴北缘早古生代两次构造-岩浆演化示意图

Fig. 10 Schematic diagram of two early Paleozoic tectonic-magmatic evolution in the North Qaidam

背景下的部分熔融相比(Yu *et al.*, 2019b),本文中长英质片麻岩的重熔发生在更浅的地壳深度,这表明即使在同一条碰撞造山带,不同区位被改造的机制与模式亦有差异。

综上,我们认为拐角梁-双口山弧岩浆-变质单元内记录的两期弧岩浆活动促进了柴北缘俯冲碰撞杂岩带陆弧地壳生长,加上随后的一期深熔事件共同推动了带内陆弧地壳向大陆地壳的转化,结合区内其他阶段的地壳生长及改造过程共同促使大陆地壳走向成熟。

6 结论

本文通过对柴北缘造山带鱼卡地区早古生代变质-岩浆杂岩进行年代学、锆石 Hf 同位素以及全岩地球化学研究,探讨柴北缘西段的大陆地壳改造和成熟过程,得到以下结论:

(1) 锆石 U-Pb 年代学和 Hf 同位素地球化学研究表明基性岩浆在 470 Ma 结晶,并发生结晶分异生成长英质岩浆,随后两者在 440 Ma 发生深熔-变质作用;

(2) 鱼卡地区 440 Ma 闪长岩是流体交代幔源物质部分熔融形成的,其岩浆侵位过程中为原有的基性和长英质地壳的深熔-变质作用提供了额外的热量和流体供应;

(3) 早古生代变质-岩浆杂岩记录了碰撞带大陆地壳的改造和成熟过程,俯冲过程中,早奥陶世幔源岩浆熔融生成的弧岩浆经历结晶分异,推动大陆地壳向长英质地壳演化;在随后陆-陆碰撞过程中,先存地壳发生深熔-变质作用,再次推动大陆地壳成熟。

References

Annen C, Blundy J D and Sparks R S J. 2006. The genesis of intermediate and silicic magmas in deep crustal hot zones[J]. Journal of Petrology, 47(3): 505~539.

Arculus R J. 1981. Island arc magmatism in relation to the evolution of the crust and mantle[J]. Tectonophysics, 75(1~2): 113~133.

Bachmann O and Huber C. 2016. Silicic magma reservoirs in the earth's crust[J]. American Mineralogist, 101(11): 2 377~2 404.

Barker F. 1979. Trondhjemite: Definition, environment and hypotheses of origin[C]// Barker F. Trondhjemites, Dacites, and Related Rocks. Amsterdam: Elsevier, 1~12.

Bartoli O. 2021. Granite geochemistry is not diagnostic of the role of water in the source [J]. Earth and Planetary Science Letters, 564: 116927.

Becker A, Holtz F and Johannes W. 1998. Liquidus temperatures and phase compositions in the system Qz-Ab-Or at 5 kbar and very low water activities[J]. Contributions to Mineralogy and Petrology, 130: 213~224.

Berndt C, Bünz S, Clayton T, *et al*. 2004. Seismic character of bottom simulating reflectors: Examples from the mid-Norwegian margin[J]. Marine and Petroleum Geology, 21(6): 723~733.

Blichert-Toft J and Albarède F. 1997. The Lu-Hf geochemistry of chondrites and the evolution of the mantle-crust system[J]. Earth and Planetary Science Letters, 148: 243~258.

Brophy J G. 2008. A study of rare earth element (REE)-SiO_2 variations in felsic liquids generated by basalt fractionation and amphibolite melting: A potential test for discriminating between the two different processes[J]. Contributions to Mineralogy and Petrology, 156: 337~357.

Brophy J G. 2009. La-SiO_2 and Yb-SiO_2 systematics in mid-ocean ridge magmas: Implications for the origin of oceanic plagiogranite[J]. Contributions to Mineralogy and Petrology, 158(1): 99~111.

Brown M. 2013. Granite: From genesis to emplacement[J]. Geological Society of America Bulletin, 125: 1 079~1 113.

Cai P J, Chen X, Majka J, *et al*. 2021. Two stages of crust-mantle interaction during oceanic subduction to continental collision: Insights from mafic-ultramafic complexes in the North Qaidam orogen[J]. Gondwana Research, 89: 247~264.

Cao Y T, Liu L, Chen D L, *et al*. 2017. Partial melting during exhumation of Paleozoic retrograde eclogite in North Qaidam, western China [J]. Journal of Asian Earth Sciences, 148: 223~240.

Castro A. 2013. Tonalite-granodiorite suites as cotectic systems: A review of experimental studies with applications to granitoid petrogenesis [J]. Earth-Science Reviews, 124: 68~95.

Castro A, Vogt K and Gerya T. 2013. Generation of new continental crust by sublithospheric silicic-magma relamination in arcs: A test of Taylor's andesite model[J]. Gondwana Research, 23(4): 1 554~1 566.

Cawood P A, Hawkesworth C J and Dhuime B. 2013. The continental record and the generation of continental crust[J]. Geological Society of America Bulletin, 125: 14~32.

Chen D L, Liu L, Sun Y, *et al*. 2012. Felsic veins within UHP eclogite at Xitieshan in North Qaidam, NW China: Partial melting during exhumation[J]. Lithos, 136: 187~200.

Chen D L, Sun Y, Liu L, *et al*. 2007. In situ LA-ICP-MS zircon U-Pb age of ultrahigh-pressure eclogites in the Yukahe area, northern Qaidam Basin[J]. Science in China Series D: Earth Sciences, 50(Suppl2): 322~330.

Chen Y X, Zheng Y F and Hu Z. 2013. Synexhumation anatexis of ultrahigh-pressure metamorphic rocks: Petrological evidence from granitic gneiss in the Sulu orogen[J]. Lithos, 156: 69~96.

Chu N C, Taylor R N and Chavagnac V. 2002. Hf isotope ratio analysis using multi-collector inductively coupled plasma mass spectrometry: An evaluation of isobaric interference corrections[J]. Journal of Analytical Atomic Spectrometry, 17: 1 567~1 574.

Davidson J P and Arculus R J. 2006. The significance of Phanerozoic arc magmatism in generating continental crust[C]// Brown M & Rushmer T. Evolution and Differentiation of the Continental Crust. New York: Cambridge University Press, 135~172.

Elhlou S, Belousova E and Griffin W L. 2006. Trace element and isotopic composition of GJ-red zircon standard by laser ablation [J]. Geochimica et Cosmochimica Acta, 70: A158.

Ferreira A C, Dantas E L, Fuck R A, *et al*. 2020. Arc accretion and crustal reworking from late Archean to Neoproterozoic in Northeast Brazil[J]. Scientific Reports, 10(1): 7 855.

France L, Koepke J, Ildefonse B, *et al*. 2010. Hydrous partial melting in the sheeted dike complex at fast spreading ridges: Experimental and natural observations[J]. Contributions to Mineralogy and Petrology, 160: 683~704.

Furnes H and Dilek Y. 2017. Geochemical characterization and petrogenesis of intermediate to silicic rocks in ophiolites: A global synthesis [J]. Earth-Science Reviews, 166: 1~37.

Gao L E, Zeng L and Asimow P D. 2017. Contrasting geochemical signatures of fluid-absent versus fluid-fluxed melting of muscovite in metasedimentary sources: The Himalayan leucogranites[J]. Geology, 45 (1): 39~42.

Gao X Y, Yu S Y, Li S Z, *et al*. 2022. Syn-collisional I-type granitoids linked to lateral lithospheric heterogeneity: A case study from the North Qaidam orogen, NW China[J]. Journal of Asian Earth Sciences, 237: 105363.

Gao X Y, Yu S Y, Li S Z, *et al*. 2023. Consecutive underplating of cognate magmas: Contributions to the enclaves and large-volume plagiogranites in the North Qaidam orogen (NW China)[J]. Lithos, 442: 107085.

Gao X Y, Yu S Y, Peng Y B, *et al*. 2021. Insights into OIB-like magmatism contemporaneous with oceanic subduction: Petrogenetic constraints on the Kendelong metagabbro in the North Qaidam[J]. Lithos, 392: 106130.

Greene A R, DeBari S M, Kelemen P B, *et al*. 2006. A detailed geochemical study of Island Arc Crust: The Talkeetna Arc Section, South-Central Alaska[J]. Journal of Petrology, 47: 1 051~1 093.

Griffin W L, Pearson N J, Belousova E, *et al*. 2000. The Hf isotope composition of cratonic mantle: LA-MC-ICPMS analysis of zircon megacrysts in kimberlites[J]. Geochimica et Cosmochimica Acta, 64(1): 133~147.

Griffin W L, Wang X, Jackson S E, *et al*. 2002. Zircon chemistry and magma mixing, SE China: In-situ analysis of Hf isotopes, Tonglu and Pingtan igneous complexes[J]. Lithos, 61: 237~269.

Hacker B R, Kelemen P B and Behn M D. 2011. Differentiation of the continental crust by relamination[J]. Earth and Planetary Science Letters, 307: 501~516.

Hawkesworth C J and Kemp A I S. 2006. Evolution of the continental crust[J]. Nature, 443: 811~817.

Hernúndez-Uribe D, Palin R M, Cone K A, *et al*. 2021. Petrological implications of seafloor hydrothermal alteration of subducted mid-ocean ridge BasaltAvailable for purchase[J]. Journal of Petrology, 61(9): egaa086.

Herzberg C. 2006. Petrology and thermal structure of the Hawaiian plume from Mauna Kea volcano[J]. Nature, 444(7 119): 605~609.

Hill E, Blundy J D and Wood B J. 2011. Clinopyroxene-melt trace element partitioning and the development of a predictive model for HFSE and Sc[J]. Contributions to Mineralogy and Petrology, 161(3): 423~438.

Hofmann A W and Jochum K P. 1996. Source characteristics derived from very incompatible trace elements in Mauna Loa and Mauna Kea basalts, Hawaii Scientific Drilling Project[J]. Journal of Geophysical Research: Solid Earth, 101(B5): 11 831~11 839.

Hofmann A W, Jochum K P, Seufert M, *et al*. 1986. Nb and Pb in oceanic basalts: New constraints on mantle evolution[J]. Earth and Planetary Science Letters, 79: 33~45.

Holness M B, Cesare B and Sawyer E W. 2011. Melted rocks under the microscope: Microstructures and their interpretation[J]. Elements, 7: 247~252.

Hou Kejun, Li Yanhe and Tian Yourong. 2009. In situ U-Pb zircon dating using laser ablation-multi ion counting-ICP-MS[J]. Mineral Deposits, 28: 481~492 (in Chinese with English abstract).

Hou Kejun, Li Yanhe, Zou Tianren, *et al*. 2007. Laser ablation-MC-ICP-MS technique for Hf isotope microanalysis of zircon and its geological applications[J]. Acta Petrologica Sinica, 23(10): 2 595~2 604(in Chinese with English abstract).

Inger S and Harris N. 1993. Geochemical constraints on leucogranite magmatism in the Langtang Valley, Nepal Himalaya[J]. Journal of Petrology, 34(2): 345~368.

Jackson M G, Hart S R, Koppers A A, *et al*. 2007. The return of subducted continental crust in Samoan lavas[J]. Nature, 448(7 154): 684~687.

Jagoutz O E. 2014. Arc crustal differentiation mechanisms[J]. Earth and Planetary Science Letters, 396: 267~277.

Jagoutz O E. 2010. Construction of the granitoid crust of an island arc. Part II: A quantitative petrogenetic model[J]. Contributions to Mineralogy and Petrology, 160(3): 359~381.

Jochum K P, McDonough W F, Palme H, *et al*. 1989. Compositional constraints on the continental lithospheric mantle from trace elements in spinel peridotite xenoliths[J]. Nature, 340: 548~550.

Jull M and Kelemen P Á. 2001. On the conditions for lower crustal convective instability[J]. Journal of Geophysical Research: Solid Earth, 106(B4): 6 423~6 446.

Kelemen P B, Hanghøj K and Greene A R. 2014. One view of the geochemistry of subduction-related magmatic arcs, with an emphasis on primitive andesite and lower crust[C]//Treatise on Geochemistry. Elsevier, 794~806.

Kelemen P B, Hanghøj K and Greene A R. 2003a. One view of the geochemistry of subduction-related magmatic arcs, with an emphasis on primitive andesite and lower crust[J]. Treatise on Geochemistry, 3: 659.

Kelemen P B, Yogodzinski G M and Scholl D W. 2003b. Along-strike variation in the Aleutian island arc: Genesis of high $Mg^{\#}$ andesite and implications for continental crust[J]. Inside the Subduction Factory, 138: 223~276.

Knesel K M and Davidson J P. 2002. Insights into collisional magmatism from isotopic fingerprints of melting reactions[J]. Science, 296(5 576): 2 206~2 208.

Koepke J, Berndt J, Feig S T, *et al*. 2007. The formation of SiO_2-rich melts within the deep oceanic crust by hydrous partial melting of gabbros[J]. Contributions to Mineralogy and Petrology, 153: 67~84.

Koepke J, Feig S and Snow J. 2004. Petrogenesis of oceanic plagiogranites by partial melting of gabbros: An experimental study[J]. Contributions to Mineralogy and Petrology, 146(4): 414~432.

Koepke J, Feig S and Snow J. 2005. Late stage magmatic evolution of oceanic gabbros as a result of hydrous partial melting: Evidence from the Ocean Drilling Program (ODP) Leg 153 drilling at the Mid-

Atlantic Ridge[J]. Geochemistry, Geophysics, Geosystems, 6(2): GC000805.

Korenaga J. 2018. Estimating the formation age distribution of continental crust by unmixing zircon ages[J]. Earth and Planetary Science Letters, 482: 388~395.

LaFlèche M R, Camire G and Jenner G A. 1998. Geochemistry of post-Acadian, Carboniferous continental intraplate basalts from the Maritimes basin, Magdalen islands, Quebec, Canada[J]. Chemical Geology, 148: 115~136.

Lappin A R and Hollister L S. 1980. Partial melting in the central gneiss complex near Prince Rupert, British Columbia[J]. American Journal of Science, 280(6): 518~545.

Lee C A, Morton D M, Kistler R W, *et al*. 2007. Petrology and tectonics of Phanerozoic continent formation: From island arcs to accretion and continental arc magmatism[J]. Earth and Planetary Science Letters, 263(3~4): 370~387.

Lee Y Y and Cho M S. 2020. Fluid-present partial melting of Paleoproterozoic Okbang amphibolite in the Yeongnam Massif, Korea[J]. Lithosphere, (1): 8854615.

Lee Y Y, Cho M S, Kim T, *et al*. 2021. Incipient charnockite formation at the waning stage of Paleoproterozoic hot orogenesis, Yeongnam Massif, Korea[J]. Precambrian Research, 365: 106388.

Li X C, Niu M L, Yakymchuk C, *et al*. 2018. Anatexis of former arc magmatic rocks during oceanic subduction: A case study from the North Wulan gneiss complex[J]. Gondwana Research, 61: 128~149.

Li X C, Niu M L, Yan Z, *et al*. 2022. Early Paleozoic continental arc mafic magmatism in the North Qaidam tectonic belt: Implications for subduction of the Proto-Tethyan oceanic lithosphere[J]. Lithosphere, (1): 3011662.

Ma Chao, Tang Yanjie and Ying Jifeng. 2019. Magmatism in subduction zones and growth of continental crust[J]. Earth Science, 44(4): 1 128~1 142(in Chinese with English abstract).

Ma Xudong and Chen Danling. 2006. Zircon LA-ICP-MS dating of felsic gneiss in the surrounding rock of UHP metamorphic rock in the northern margin of Qaidam basin[J]. Geological Bulletin of China, 25(S1): 99~103(in Chinese).

McDermott F, Harris N B W and Hawkesworth C J. 1996. Geochemical constraints on crustal anatexis: A case study from the Pan-African Damara granitoids of Namibia[J]. Contributions to Mineralogy and Petrology, 123: 406~423.

McLellan E L. 1988. Migmatite structures in the Central Gneiss Complex, Boca de Quadra, Alaska[J]. Journal of Metamorphic Geology, 6(4): 517~542.

Middlemost E A. 1994. Naming materials in the magma/igneous rock system[J]. Earth-science Reviews, 37(3~4): 215~224.

Müntener O and Ulmer P. 2006. Experimentally derived high-pressure cumulates from hydrous arc magmas and consequences for the seismic velocity structure of lower arc crust[J/OL]. Geophysical Research Letters, 33(21). DOI: 10.1029/2006GL027629.

Niu Y L, Zhao Z D, Zhu D C, *et al*. 2013. Continental collision zones are primary sites for net continental crust growth: A testable hypothesis[J]. Earth-Science Reviews, 127: 96~110.

Niu Y and O'Hara M J. 2009. MORB mantle hosts the missing Eu (Sr, Nb, Ta and Ti) in the continental crust: New perspectives on crustal growth, crust-mantle differentiation and chemical structure of oceanic upper mantle[J]. Lithos, 112(1~2): 1~17.

Pang Ajuan, Li Shengrong, Zhang Huafeng, *et al*. 2012. Genetic mineralogy significance of major minerals of Jilongshan pluton, Hubei province[J]. Journal of Mineralogy and Petrology, 32(3): 25~33 (in Chinese with English abstract).

Patiño-Douce A E. 1996. Effects of pressure and H_2O content on the compositions of primary crustal melts[J]. Earth and Environmental Science Transactions of the Royal Society of Edinburgh, 87(1~2): 11~21.

Patiño-Douce A E. 2005. Vapor-absent melting of tonalite at 15~32 kbar[J]. Journal of Petrology, 46: 275~290.

Patiño-Douce A E and Beard J S. 1995. Dehydration-melting of biotite gneiss and quartz amphibolite from 3 to 15 kbar[J]. Journal of Petrology, 36: 707~738.

Patiño-Douce A E and Harris N. 1998. Experimental constraints on Himalayan anatexis[J]. Journal of petrology, 39(4): 689~710.

Pichavant M, Holtz F and McMillan P F. 1992. Phase relations and compositional dependence of H_2O solubility in quartz-feldspar melts[J]. Chemical Geology, 96(3~4): 303~319.

Qin Shengkai, Zhang Zeming and Zhang Ronghui. 2023. Petrogenesis and tectonic significance of the Early Miocene adakitic granites from the Quxu area, Gangdese magmatic arc[J]. Acta Petrologica et Mineralogica, 42(3): 329~349(in Chinese with English abstract).

Reichardt H, Weinberg R F, Andersson U B, *et al*. 2010. Hybridization of granitic magmas in the source: The origin of the Karakoram Batholith, Ladakh, NW India[J]. Lithos, 116(3~4): 249~272.

Ren Y F, Chen D L, Kelsey D E, *et al*. 2017. Petrology and geochemistry of the lawsonite (pseudomorph)-bearing eclogite in Yuka terrane, North Qaidam UHPM belt: An eclogite facies metamorphosed oceanic slice[J]. Gondwana Research, 42: 220~242.

Ren Y F, Chen D L, Zhu X H, *et al*. 2019. Two orogenic cycles recorded by eclogites in the Yuka-Luofengpo terrane: Implications for the Mesoproterozoic to early Paleozoic tectonic evolution of the North Qaidam orogenic belt, NW China[J]. Precambrian Research, 333: 105~449.

Rudnick R L. 1995. Making continental crust[J]. Nature, 378: 571~578.

Rudnick R L and Gao S. 2003. Composition of the continental crust[J]. Treatise on Geochemistry, 3: 659.

Sawyer E W. 2008. Atlas of migmatites[J]. Canadian Mineralogist, 46: 1 373~1 374.

Schorn S, Hartnady M I, Diener J F, *et al*. 2021. H_2O-fluxed melting of eclogite during exhumation: An example from the eclogite type-locality, Eastern Alps (Austria)[J]. Lithos, 390: 106~118.

Shi Rendeng, Yang Jingsui, Wu Cailai, *et al*. 2004. Island arc volcanic rocks in the north Qaidam UHP metamorphic belt[J]. Acta Geologica Sinica, 78(1): 52~64(in Chinese with English abstract).

Sobolev A V, Hofmann A W, Kuzmin D V, *et al*. 2007. The amount of recycled crust in sources of mantle-derived melts[J]. Science, 316 (5 823): 412~417.

Söderlund U, Patchett P J, Vervoort J D, *et al*. 2004. The 176Lu decay constant determined by Lu-Hf and U-Pb isotope systematics of Precambrian manfic intrusions[J]. Earth and Planetary Science Letters, 219(3~4): 311~324.

Song S G, Niu Y L, Su L, *et al*. 2014a. Adakitic (tonalitic-trondhjemitic) magmas resulting from eclogite decompression and dehydration melting during exhumation in response to continental collision[J]. Geochimica et Cosmochimica Acta, 130: 42~62.

Song S G, Niu Y L, Su L, *et al*. 2014b. Continental orogenesis from ocean subduction, continent collision/subduction, to orogen collapse, and orogen recycling: The example of the North Qaidam UHPM belt, NW China[J]. Earth-Science Reviews, 129: 59~84.

Song S G, Wang M J, Wang C, *et al*. 2015. Magmatism during continental collision, subduction, exhumation and mountain collapse in collisional orogenic belts and continental net growth: A perspective[J]. Science China Earth Sciences, 58: 1 284~1 304.

Spencer C J, Roberts N M W and Santosh M. 2017. Growth, destruction, and preservation of Earth's continental crust[J]. Earth-Science Reviews, 172: 87~106.

Sun G C, Gao P, Zhao Z F, *et al*. 2020. Syn-exhumation melting of the subducted continental crust: Geochemical evidence from early Paleozoic granitoids in North Qaidam, northern Tibet[J]. Lithos, 374: 105707.

Sun S S and McDonough W F. 1989. Chemical and isotopic systematics of oceanic basalts: Implications for mantle composition and processes [J]. Geological Society, London, Special Publications, 42(1): 313~345.

Tamura Y, Sato T, Fujiwara T, *et al*. 2016. Advent of continents: A new hypothesis[J]. Scientific Reports, 6(1): 33 517.

Tang Yue, Zhai Qingguo, Hu Peiyuan, *et al*. 2021. Petrogenesis of anorthosite in the Laguoco ophiolite, western part of the BangongNujiang suture zone and its constraint to the evolution of the Meso-Tethys Ocean[J]. Geological Bulletin of China, 40(8): 1 265~1 278 (in Chinese with English abstract).

Taylor S R. 1967. The origin and growth of continents[J]. Tectonophysics, 4: 17~34.

Taylor S R and McLennan S M. 1995. The geochemical evolution of the continental crust[J]. Reviews of geophysics, 33(2): 241~265.

Thompson A B and Connolly J A. 1995. Melting of the continental crust: some thermal and petrological constraints on anatexis in continental collision zones and other tectonic settings[J]. Journal of Geophysical Research: Solid Earth, 100(B8): 15 565~15 579.

Wang Bingzhang, Fu Changlei, Pan Tong, *et al*. 2022. Early Paleozoic magmatism in the Saishiteng area, North Qaidam and their constraint on tectonic evolution[J]. Acta Petrologica Sinica, 38(9): 2 723~2 742(in Chinese with English abstract).

Wang Q Y, Dong Y J, Pan Y M, *et al*. 2018. Early Paleozoic granulite-facies metamorphism and magmatism in the northern Wulan terrane of the Quanji massif: Implications for the evolution of the proto-Tethys Ocean in northwestern China[J]. Journal of Earth Science, 29: 1 081~1 101.

Wang Zhenqiang, Zhang Zhaowei, Ding Peichao, *et al*. 2022. Geochronology, geochemistry and significance of the metabasic volcanic rocks in Tuomoerrite area, North Qaidam[J]. Acta Petrologica et Mineralogica, 41(3): 491~503(in Chinese with English abstract).

Watt G R and Harley S L. 1993. Accessory phase controls on the geochemistry of crustal melts and restites produced during water-undersaturated partial melting[J]. Contributions to Mineralogy and Petrology, 114(4): 550~566.

Weinberg R F and Hasalová P. 2015. Water-fluxed melting of the continental crust: A review[J]. Lithos, 212: 158~188.

Wu C L, Gao Y H, Li Z L, *et al*. 2014. Zircon SHRIMP U-Pb dating of granites from Dulan and the chronological framework of the North Qaidam UHP belt, NW China[J]. Science China Earth Sciences, 57(12): 2 945~2 965.

Wu C L, Wooden J L, Robinson P T, *et al*. 2009. Geochemistry and zircon SHRIMP U-Pb dating of granitoids from the west segment of the North Qaidam[J]. Science in China Series D: Earth Sciences, 52 (11): 1 771~1 790.

Wu C L, Wooden J L, Yang J S, *et al*. 2006. Granitic magmatism in the North Qaidam early Paleozoic ultrahigh-pressure metamorphic belt, northwest China[J]. International Geology Review, 48(3): 223~240.

Wu Yuanbao and Zheng Yongfei. 2004. Genetic mineralogy of zircon and its constraints on U-Pb age interpretation[J]. Chinese Science Bulletin, 49(16): 1 589~1 604(in Chinese).

Yakymchuk C, Zhao W R, Wan Y S, *et al*. 2019. Fluid-present anatexis of Neoarchean tonalite and amphibolite in the Western Shandong Province[J]. Lithos, 326: 110~124.

Yang H, Zhang H F, Luo B J, *et al*. 2016. Generation of peraluminous granitic magma in a post-collisional setting: A case study from the eastern Qilian orogen, NE Tibetan Plateau[J]. Gondwana Research, 36: 28~45.

Yang Jingsui, Zhang Jianxin, Meng Fancong, *et al*. 2003. Ultrahigh pressure eclogites of the north Qaidam and altun mountains, NW China and their protoliths[J]. Earth Science Frontiers, 10(3): 291~314(in Chinese with English abstract).

Yang S X, Su L, Song S G, *et al*. 2020. Melting of subducted continental crust during collision and exhumation: Insights from granitic rocks from the North Qaidam UHP metamorphic belt, NW China[J]. Lithos, 378: 105794.

Yang Z F and Zhou J H. 2013. Can we identify source lithology of basalt? [J]. Scientific Reports, 3(1): 1 856.

Yu Junzhen, Zheng Youye and Xu Rongke. 2020. LA-ICP-MS zircon U-Pb age of the host rock and hydrothermal zircon in gold-bearing quartz vein of Shuangkoushan Au-Ag-Pb deposit, North Qaidam: Limitation for the mineralization age and implication for the genesis of the deposit[J]. Acta Geologica Sinica, 94(11): 3 361~3 375(in Chinese with English abstract).

Yu S Y, Li S Z, Zhang J X, *et al*. 2019a. Linking high-pressure mafic granulite, TTG-like (tonalitic-trondhjemitic) leucosome and pluton, and crustal growth during continental collision[J]. Geological Society of America Bulletin, 131(3~4): 572~586.

Yu S Y, Li S Z, Zhang J X, *et al*. 2019b. Multistage anatexis during tectonic evolution from oceanic subduction to continental collision: A review of the North Qaidam UHP Belt, NW China[J]. Earth-Science Reviews, 191: 190~211.

Yu S Y, Peng Y B, Zhang J X, *et al*. 2021. Tectono-thermal evolution of the Qilian orogenic system: Tracing the subduction, accretion and closure of the Proto-Tethys Ocean[J]. Earth-Science Reviews, 215: 103547.

Yu S Y, Zhang J X, Del Real P G. 2012. Geochemistry and zircon U-Pb ages of adakitic rocks from the Dulan area of the North Qaidam UHP terrane, north Tibet: Constraints on the timing and nature of regional tectonothermal events associated with collisional orogeny[J]. Gondwana Research, 21(1): 167~179.

Yu S Y, Zhang J X, Li H K, *et al*. 2013. Geochemistry, zircon U-Pb geochronology and Lu-Hf isotopic composition of eclogites and their host gneisses in the Dulan area, North Qaidam UHP terrane: New evidence for deep continental subduction[J]. Gondwana Research, 23(3): 901~919.

Yu S Y, Zhang J X, Li S Z, *et al*. 2019c. TTG-adakitic-like (tonalitic-trondhjemitic) magmas resulting from partial melting of metagabbro under high-pressure condition during continental collision in the North Qaidam UHP terrane, western China[J]. Tectonics, 38 (3): 791~822.

Yu S Y, Zhang J X, Qin H P, *et al*. 2015a. Petrogenesis of the early Paleozoic low-Mg and high-Mg adakitic rocks in the North Qilian orogenic belt, NW China: Implications for transition from crustal thickening to extension thinning[J]. Journal of Asian Earth Sciences, 107: 122~139.

Yu S Y, Zhang J X, Sun D Y, *et al*. 2015b. Petrology, geochemistry, zircon U-Pb dating and Lu-Hf isotope of granitic leucosomes within felsic gneiss from the North Qaidam UHP terrane: Constraints on the timing and nature of partial melting[J]. Lithos, 218: 1~21.

Yu S Y, Zhang J X, Sun D Y, *et al*. 2015c. Anatexis of ultrahigh-pressure eclogite during exhumation in the North Qaidam ultrahigh-pressure terrane: Constraints from petrology, zircon U-Pb dating, and geochemistry[J]. Geological Society of America Bulletin, 127(9~10): 1 290~1 312.

Yuan Guibang, Wang Huichu, Li Huimin, *et al*. 2002. Zircon U-Pb age of the gabbros in luliangshan area on the northern margin of Qaidam basin and its geological implication[J]. Progress in Precambrian Research, 25(1): 36~38, 37~40(in Chinese with English abstract).

Zeng L, Asimow P D and Saleeby J B. 2005. Coupling of anatectic reactions and dissolution of accessory phases and the Sr and Nd isotope systematics of anatectic melts from a metasedimentary source[J]. Geochimica et Cosmochimica Acta, 69(14): 3 671~3 682.

Zhang C, Zhang L F, Van Roermund H V, *et al*. 2011. Petrology and SHRIMP U-Pb dating of Xitieshan eclogite, North Qaidam UHP metamorphic belt, NW China[J]. Journal of Asian Earth Sciences, 42 (4): 752~767.

Zhang G, Zhang L and Christy A G. 2013. From oceanic subduction to continental collision: An overview of HP-UHP metamorphic rocks in the North Qaidam UHP belt, NW China[J]. Journal of Asian Earth Sciences, 63: 98~111.

Zhang G B, Ellis D J, Christy A G, *et al*. 2009b. UHP metamorphic evolution of coesite-bearing eclogite from the Yuka terrane, North Qaidam UHPM belt, NW China[J]. European Journal of Mineralogy, 21(6): 1 287~1 300.

Zhang G B, Han L, Zhang L F, *et al*. 2023. The transition from oceanic to continental subduction and collision: A case study of the North Qaidam ultrahigh-pressure metamorphic belt, northern Tibetan Plateau[J]. Journal of Asian Earth Sciences, 242: 105488.

Zhang G B, Ireland T, Zhang L F, *et al*. 2016. Zircon geochemistry of two contrasting types of eclogite: Implications for the tectonic evolution of the North Qaidam UHPM belt, northern Tibet[J]. Gondwana Research, 35: 27~39.

Zhang G B, Song S G, Zhang L F, *et al*. 2008a. The subducted oceanic crust within continental-type UHP metamorphic belt in the North Qaidam, NW China: Evidence from petrology, geochemistry andgeochronology[J]. Lithos, 104(1~4): 99~118.

Zhang G B, Zhang L F, Song S G, *et al*. 2009a. UHP metamorphic evolution and SHRIMP geochronology of a coesite-bearing metaophiolitic gabbro in the North Qaidam, NW China[J]. Journal of Asian Earth Sciences, 35(3~4): 310~322.

Zhang J X, Mattinson C G, Meng F C, *et al*. 2008b. Polyphase tectonothermal history recorded in granulitized gneisses from the North Qaidam HP/UHP metamorphic terrane, western China: Evidence from zircon U-Pb geochronology[J]. Geological Society of America Bulletin, 120(5~6): 732~749.

Zhang J X, Mattinson C G, Yu S Y, *et al*. 2010. U-Pb zircon geochronology of coesite-bearing eclogites from the southern Dulan area of the North Qaidam UHP terrane, northwestern China: Spatially and temporally extensive UHP metamorphism during continental subduction [J]. Journal of Metamorphic Geology, 28: 955~978.

Zhang Jianxin, Yu Shengyao, Li Yunshuai, *et al*. 2015. Subduction, accretion and closure of proto-Tethyan ocean: Early Paleozoic accretion/collision orogeny in the altun-Qilian-north Qaidam Orogenic system[J]. Acta Petrologica Sinica, 31(12): 3 531~3 554(in Chinese with English abstract).

Zhang L, Chen R X, Zheng Y F, *et al*. 2017. Whole-rock and zircon geochemical distinction between oceanic- and continental-type eclogites in the North Qaidam orogen, northern Tibet[J]. Gondwana Research, 44: 67~88.

Zhang Z M, Dong X, Xiang H, *et al*. 2014. Metagabbros of the Gangdese arc root, south Tibet: Implications for the growth of continental crust [J]. Geochimica et Cosmochimica Acta, 143: 268~284.

Zhao Z X, Wei J H, Fu L B, *et al*. 2017. The Early Paleozoic Xitieshan syn-collisional granite in the North Qaidam ultrahigh-pressure metamorphic belt, NW China: Petrogenesis and implications for continental crust growth[J]. Lithos, 278: 140~152.

Zheng Y F. 2012. Metamorphic chemical geodynamics in continental subduction zones[J]. Chemical Geology, 328: 5~48.

Zheng Y F and Gao P. 2021. The production of granitic magmas through crustal anatexis at convergent plate boundaries[J]. Lithos, 402: 106232.

Zheng Y F, Zhao Z F, Wu Y B, *et al*. 2006. Protolith nature of deeply subducted continent: Zircon U-Pb age, Hf and O isotope constraints from UHP eclogite and gneiss in the Dabie orogen[J]. Geochimica et Cosmochimica Acta, 18(70): A745.

Zhou G S, Zhang J X, Mattinson C G, *et al*. 2022. Exhumation of deeply subducted continental crust along contrasting pathways: Examples from the North Qaidam ultrahigh pressure metamorphic terrane, North Tibet[J]. Gondwana Research, 103: 221~242.

Zhu D C, Wang Q, Weinberg R F, *et al*. 2022. Interplay between oceanic subduction and continental collision in building continental crust [J]. Nature Communications, 13: 7 141.

Zhu Xiaohui, Chen Danling, Liu Liang, *et al*. 2014. Geochronology, geochemistry and significance of the Early Paleozoic back-arc type ophiolite in Lvliangshan area, North Qaidam[J]. Acta Petrologica Sinica, 30(3): 822~834(in Chinese with English abstract).

Zhu Xiaohui, Chen Danling, Wang Chao, *et al*. 2015. The initiation, development and termination of the Neoproterozoic-early Paleozoic Ocean in the northern margin of Qaidam basin[J]. Acta Geologica Sinica, 89(2): 234~251(in Chinese with English abstract).

附中文参考文献

侯可军, 李延河, 田有荣. 2009. LA-MC-ICP-MS 锆石微区原位 U-Pb 定年技术[J]. 矿床地质, 28(4): 481~492.

侯可军, 李延河, 邹天人, 等. 2007. LA-MC-ICP-MS 锆石 Hf 同位素的分析方法及地质应用[J]. 岩石学报, 23(10): 2 595~2 604.

马 超, 汤艳杰, 英基丰. 2019. 俯冲带岩浆作用与大陆地壳生长[J]. 地球科学, 44(4): 1 128~1 142.

马旭东, 陈丹玲. 2006. 柴达木盆地北缘超高压变质岩的围岩长英质片麻岩锆石 LA-ICP-MS 定年[J]. 地质通报, 25(S1): 99~103.

庞阿娟，李胜荣，张华锋，等. 2012. 湖北鸡笼山岩体主要矿物的成因矿物学意义[J]. 矿物岩石，32(3)：25~33.

秦圣凯，张泽明，张荣辉. 2023. 冈底斯岩浆弧曲水地区早中新世埃达克质花岗岩的成因及构造意义[J]. 岩石矿物学杂志，42(3)：329~349.

史仁灯，杨经绥，吴才来，等. 2004. 柴达木北缘超高压变质带中的岛弧火山岩[J]. 地质学报，78(1)：52~64.

唐　跃，翟庆国，胡培远，等. 2021. 班公湖-怒江缝合带西段拉果错蛇绿岩中斜长岩成因及其对中特提斯洋演化的制约[J]. 地质通报，40(8)：1 265~1 278.

王秉璋，付长垒，潘　彤，等. 2022. 柴北缘赛什腾地区早古生代岩浆活动与构造演化[J]. 岩石学报，38(9)：2 723~2 742.

王振强，张照伟，丁培超，等. 2022. 柴北缘托莫尔日特地区变基性火山岩年代学、地球化学特征及地质意义[J]. 岩石矿物学杂志，41(3)：491~503.

吴元保，郑永飞. 2004. 锆石成因矿物学研究及其对 U-Pb 年龄解释的制约[J]. 科学通报，49(16)：1 589~1 604.

杨经绥，张建新，孟繁聪，等. 2003. 中国西部柴北缘—阿尔金的超高压变质榴辉岩及其原岩性质探讨[J]. 地学前缘，10(3)：291~314.

俞军真，郑有业，许荣科. 2020. 柴北缘双口山金-银-铅矿床赋矿围岩及含金石英脉热液锆石 U-Pb 定年对成矿时代的限定及其成因启示[J]. 地质学报，94(11)：3 361~3 375.

袁桂邦，王惠初，李惠民，等. 2002. 柴北缘绿梁山地区辉长岩的锆石 U-Pb 年龄及意义[J]. 前寒武纪研究进展，25(1)：36~38，37~40.

张建新，于胜尧，李云帅，等. 2015. 原特提斯洋的俯冲、增生及闭合：阿尔金-祁连-柴北缘造山系早古生代增生/碰撞造山作用[J]. 岩石学报，31(12)：3 531~3 554.

朱小辉，陈丹玲，刘　良，等. 2014. 柴北缘绿梁山地区早古生代弧后盆地型蛇绿岩的年代学、地球化学及大地构造意义[J]. 岩石学报，30(3)：822~834.

朱小辉，陈丹玲，王　超，等. 2015. 柴达木盆地北缘新元古代-早古生代大洋的形成、发展和消亡[J]. 地质学报，89(2)：234~251.